Atmos. Chem. Phys. Discuss., doi:10.5194/acp-2016-970, 2016
Manuscript under review for journal Atmos. Chem. Phys.
Published: 4 November 2016

Atmospheric Chemistry and Physics Discussions

Potential of remote sensing of cirrus optical thickness by airborne spectral radiance measurements in different viewing angles and nadir geometry

Kevin Wolf[1], André Ehrlich[1], Tilman Hüneke[2], Klaus Pfeilsticker[2], Frank Werner[1,3], Martin Wirth[4], and Manfred Wendisch[1]

[1]Leipzig Institute for Meteorology, University of Leipzig, Leipzig, Germany

[2]Institute of Environmental Physics, University of Heidelberg, Heidelberg, Germany

[3]now at Joint Center for Earth Systems Technology, University of Maryland, Baltimore, MD, USA

[4]Institute of Atmospheric Physics, German Aerospace Center, Oberpfaffenhofen, Germany

Correspondence to: K. Wolf (kevin.wolf@uni-leipzig.de)

Abstract. Spectral radiance measurements from two airborne passive solar remote sensing instruments, the Spectral Modular Airborne Radiation measurement sysTem (SMART) and the Differential Optical Absorption Spectrometer (mini-DOAS), are used to compare the remote sensing of cirrus optical thickness τ in nadir and off-nadir geometry. The comparison is based on a sensitivity study using radiative transfer simulations and on measurements during the North Atlantic Rainfall VALidation (NARVAL) mission, the Mid-Latitude Cirrus Experiment (ML-CIRRUS) and the Aerosol, Cloud, Precipitation, and Radiation Interactions and Dynamics of Convective Cloud Systems (ACRIDICON) campaign. Radiative transfer simulations are used to quantify the sensitivity of measured upward radiance I with respect to cirrus optical thickness τ, effective radius r_{eff}, viewing angle of the sensor θ_{L}, surface albedo α and ice crystal shape. From the calculations it is concluded that off-nadir measurements at wavelengths larger than λ = 900 nm significantly improve the ability to measure clouds of low optical thickness.

The comparison of nadir and off-nadir retrievals of τ from mini-DOAS, SMART and independent estimates by the Water Vapour Lidar Experiment in Space (WALES) show general agreement within the range of measurement uncertainties. For the selected example case a mean optical thickness of 0.54 $\pm$ 0.2 is derived by SMART and 0.49 $\pm$ 0.2 by mini-DOAS nadir channels, while WALES obtained a mean value of 0.32 at 532 nm respectively. The mean of τ derived from the scanning mini-DOAS channels is 0.26. For the few simultaneous measurements, the scanning mini-DOAS measurements systematically underestimate (- 17.6 %) the nadir observations from SMART and mini-DOAS, most likely due to the different probed scenes. The different values of τ derived by SMART, mini-DOAS and WALES can be potentially linked to spatial averages, ice crystal shape and the measurement strategies. The agreement of the simulations and retrievals indicate that off-nadir measurements are generally suited better to retrieve τ of thin clouds.

Atmos. Chem. Phys. Discuss., doi:10.5194/acp-2016-970, 2016
Manuscript under review for journal Atmos. Chem. Phys.
Published: 4 November 2016

Atmospheric Chemistry and Physics Discussions

1 Introduction

The impact of cirrus on the atmospheric energy budget and climate system is uncertain (IPCC, 2013), which is partly due to the limited knowledge about the formation and development of cirrus (Sausen et al., 2005). Until now it is not sufficiently quantified to what fraction homogeneous or heterogeneous ice nucleation contributes to the cirrus formation (Cziczo et al., 2013). As a result, the evolution of the cirrus microphysical properties during the life-cycle of the cirrus is insufficiently represented in climate models (IPCC, 2013). Further the globally averaged influence of cirrus on the Earth's radiation budget is highly variable because it strongly depends on their microphysical properties such as ice crystal number, size and shape (Zhang et al., 1999; Wendisch et al., 2005, 2007). Additionally, the radiative effects of different ice crystal sizes and shapes are not well quantified (Chen et al., 2000; Yang et al., 2012).

Another problem in estimating the impact of cirrus on the Earth's energy budget is the presence of sub-visible cirrus (SVC), which is difficult to observe and not well represented in the General Circulation Models (GCM) (Wiensz et al., 2013).
Despite the fact that SVC are optically thin ($\tau < 0.03$), they extend over large areas (Davis et al., 2010). Therefore, their influence on the energy budget of the Earth can not be neglected. Lee et al. (2009) estimated the annually and globally averaged radiative forcing of SVC with $+1\,\mathrm{W\,m^{-2}}$ (warming effect), while local forcings might be significantly higher. Especially, the location and time where SVC occur determine their radiative effects. Whether SVC heat or cool the atmosphere depends on surface albedo α, solar zenith angle θ_0 and cirrus optical thickness τ (Fu and Liou, 1993). In general SVC and cirrus have a heating effect at the top-of-atmosphere (TOA) since the reduction of outgoing infrared radiation usually dominates the cooling effect due to reflection of solar radiation (McFarquhar et al., 2000; Comstock et al., 2002; Davis et al., 2010).
In order to quantify better the uncertainties related to SVC, more observations of SVC appear worthwhile. Several satellite missions and field studies were performed in the past e.g., by Wang et al. (1996), Winker and Trepte (1998), Sassen et al. (2009) and Jensen et al. (2015) to establish a reliable data base on SVC. Airborne in-situ measurements by e. g., Lampert et al. (2009) Davis et al. (2010), Froyd et al. (2010) and Frey et al. (2011) were utilized to determine ice crystal size and shape of SVCs. Optical and microphysical parameters derived from these measurements are used in radiative transfer simulation and numerical weather prediction and climate modelling (Kärcher, 2002).
Despite these efforts, in-situ observations of SVC are still limited and partly accidental due to the challenge of locating SVC, e.g. Lampert et al. (2009) sampled an Arctic SVC after it was detected by an airborne lidar. Airborne campaigns dedicated to visible cirrus, e. g., Contrail, volcanoe and Cirrus Experiment (CONCERT), Mid-Latitude Cirrus (ML-CIRRUS) and tropical cirrus sampled during the Airborne Tropical TRopopause EXperiment (ATTREX) are more frequent (Delanoe et al., 2013; Ehret et al., 2014; Gross et al., 2015; Jensen et al., 2015) and occasionally include observations of SVC. Further international airborne missions like the Tropical Composition, Cloud and Climate Coupling (TC4) (Toon et al., 2010) and the Cirrus Regional Study of Tropical Anvils and Cirrus Layers - Florida Area Cirrus Experiment (CRYSTAL-FACE) mission were conducted trying to fill the knowledge gap about the formation process and physical properties of tropical cirrus (Jensen et al., 2015).
While satellite observations are suited to study the global coverage of cirrus, their spatial and temporal resolution is inherently

Atmos. Chem. Phys. Discuss., doi:10.5194/acp-2016-970, 2016
Manuscript under review for journal Atmos. Chem. Phys.
Published: 4 November 2016

Atmospheric Chemistry and Physics Discussions

limited. As a consequence of the high spatial variation of the relevant parameters the influence of different microphysical parameters, e.g., ice crystal shape, on the radiative budget of the Earth can not be studied using such coarse resolution remote sensing instrumentation. This emphasizes the need for in-situ measurements providing a large temporal and spatial resolution. As a result, airborne remote sensing is required to bridge local in-situ and global satellite observations.

For passive remote sensing of cirrus nadir and off-nadir observations are available. For nadir observations the cirrus optical thickness τ and effective radius r_{eff} of water clouds can be retrieved by the bi-spectral reflectivity method after Twomey and Seton (1980) and Nakajima and King (1990). Ou et al. (1993), Rolland et al. (2000) and King et al. (2004) adapted this method for ice clouds by introducing some modifications with regard to the thermodynamic phase and crystal shape of the ice particles. Especially due to the crystal shape and low τ cirrus retrievals lead to higher uncertainties as compared to water clouds (Eichler et al., 2009; Fricke et al., 2014).

For low τ, the reflected radiation is dominated by the surface reflection below the cirrus. This may introduce a bias in the retrieval of τ of up to $30\,\%$ when the surface albedo α is not accurately known or inhomogeneous (Fricke et al., 2014). However, even over dark surfaces the radiance reflected by the cirrus might be weak and can be in the same order of magnitude as Rayleigh scattering in the atmosphere. In addition, inhomogeneities of cirrus lead to three-dimensional (3-D) radiative effects, which may cause a bias in the one-dimensional (1-D) radiative transfer simulations (Eichler et al., 2009). Incorrectly assumed ice crystal shapes also contribute to the retrieval uncertainty. Eichler et al. (2009) investigated the influence of ice crystal shape on derived τ and r_{eff}. Evaluating a case study, they concluded that different shapes can lead to relative differences in τ of up to $70\,\%$. In summary, all these effects can render retrievals of τ to become rather inaccurate and impossible.

Off-nadir measurements of SVC and cirrus were first introduced and utilized for satellite measurements by Woodbury and McCormick (1986). Since then, several applications based on this method were developed and are not routinely be used in trace gas measurements (Wang et al., 1996; Bourassa et al., 2005; Fu et al., 2007).

Many trace gas retrievals from aircraft, balloons and satellites are based on ultraviolet (UV)/ visible (VIS)/ near infrared (SWIR) off-nadir measurements in combination with differential optical absorption spectroscopy (DOAS), e. g. performed by Platt and Stutz (2008). Compared to nadir observations, radiance measurements in off-nadir geometry are supposed to be highly sensitive to optical thin clouds due to their observation geometry. One recent study was accomplished by Wiensz et al. (2013) who used satellite off-nadir measurements especially for SVC investigation in the tropical tropopause layer (TTL). This data source improved SVC observations with respect to cloud climatology and microphysics.

In the present study, retrievals of τ based on simultaneous airborne nadir and off-nadir observations of cirrus are compared to elaborate the potential of off-nadir measurements to derive optical parameters of SVC and optically thin cirrus. This includes a sensitivity study using radiative transfer simulations (RTS) presented in Section 2 and measurements on board of the High Altitude and LOng range research aircraft (HALO) of the German Aerospace Center (DLR). With a maximum ceiling altitude of around 15 km the HALO aircraft is feasible to operate in and above SVC and cirrus in mid-latitudes and polar regions for in-situ measurements. The airborne observations are obtained with the Spectral Modular Airborne Radiation measurement sysTem (SMART) (Wendisch et al., 2001) and the Differential Optical Absorption Spectrometer (mini-DOAS) (Hüneke, 2011) both assembled on HALO. The instrumentation is introduced in Section 3. Observations from four campaigns, the Mid Latitude Cirrus experiment (ML-CIRRUS), the Next-generation Aircraft Remote sensing for Validation Studies (NARVAL North

Atmos. Chem. Phys. Discuss., doi:10.5194/acp-2016-970, 2016
Manuscript under review for journal Atmos. Chem. Phys.
Published: 4 November 2016

Atmospheric Chemistry and Physics Discussions

and South), and the Aerosol, Cloud, Precipitation, and Radiation Interactions and Dynamics of Convective Cloud Systems (ACRIDICON-CHUVA) (Wendisch et al., 2016) are used to cross-calibrate the two individual instruments in terms of absolute radiance I as presented in Section 4. In Section 5 an iterative retrieval of τ is introduced. Utilizing the cross-calibrations together with nadir and off-nadir measurements of upward I, the retrieved results are presented and compared to reference measurements of τ.

Atmos. Chem. Phys. Discuss., doi:10.5194/acp-2016-970, 2016
Manuscript under review for journal Atmos. Chem. Phys.
Published: 4 November 2016

Atmospheric Chemistry and Physics Discussions

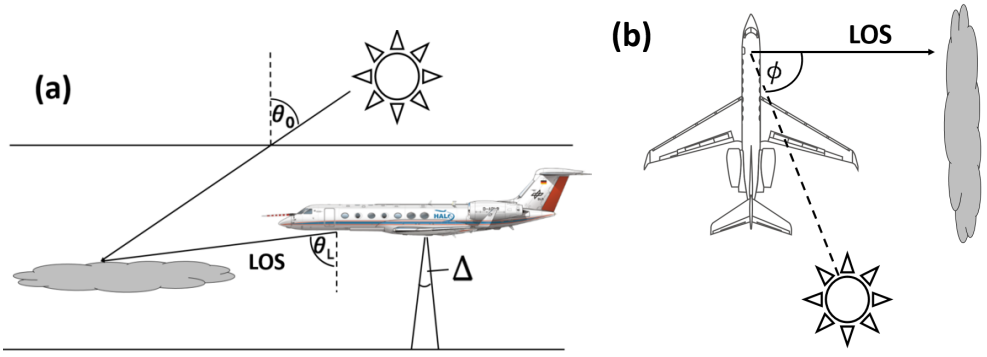

Figure 1. Illustration of the measurement geometry. (a) shows the side view with solar zenith angle θ_0 and the viewing angle θ_L. The opening angle of the nadir looking radiance sensor of SMART is indicated by Δ. Top view (b) shows the definition of the relative solar azimuth angle ϕ between the line-of-sight (LOS) and the Sun.

2 Sensitivity of remote sensing in nadir and off-nadir viewing directions

Radiative transfer simulations (RTS) are first performed to investigate the sensitivity of solar radiance measurements in nadir and off-nadir geometry for sub-visible and visible cirrus. In this way the potential of off-nadir versus nadir observations for cirrus cloud parameter detection (τ and r_{eff}) is examined.

Figure 1 illustrates the definition of the measurement geometry. The solar zenith angle (SZA) θ_0 is the angle between zenith and the Sun. The viewing angle θ_{L} describes the angle of the sensor orientation measured between the Line of Sight (LOS) and the nadir direction. For a sensor measuring in nadir θ_{L} is $0°$ and a sensor orientation close to the horizon is around $\theta_{\text{L}} \approx 90°$. The relative solar azimuth angle (RSAA) ϕ represents the angle between LOS and the Sun. It is calculated from the difference of the azimuth angle of the Sun and the azimuth angle of the observation geometry of the optical inlets. For $\phi = 0°$ the LOS is pointing directly in the direction of the Sun and with $\phi = 180°$ the LOS is looking away from the sun.

For the RTS a typical mid-latitude cirrus with a cloud base height of 10 km and a cloud top height of 12 km is assumed. Calculations are performed for $\theta_0 = 25°, 50°$ and $75°$ representing three different scenarios. The relative solar azimuth angle is set to $\phi = 0°, 90°$ and $180°$.

The simulations are performed with the radiative transfer package libRadtran 2.0 (Mayer and Kylling, 2005). The discrete ordinate radiative transfer solver (FDISORT 2) after Stamnes et al. (2000) is chosen. The incoming extraterrestrial solar flux density given by Gueymard (2004) is applied and molecular absorption is calculated using LOWTRAN (Pierluissi and Peng, 1985). For the atmospheric aerosol concentration a marine aerosol profile is chosen (Shettle, 1989) and for vertical profiles of temperature, humidity and pressure, a mid-latitude summer atmosphere profile is assumed. For the simulations a spectral albedo α typically for oceans is chosen according to the data of Clark et al. (2007). A mixture of different particle shapes is used when not other specified. The ice scattering phase function is parameterized according to Yang et al. (2013).

Atmos. Chem. Phys. Discuss., doi:10.5194/acp-2016-970, 2016
Manuscript under review for journal Atmos. Chem. Phys.
Published: 4 November 2016

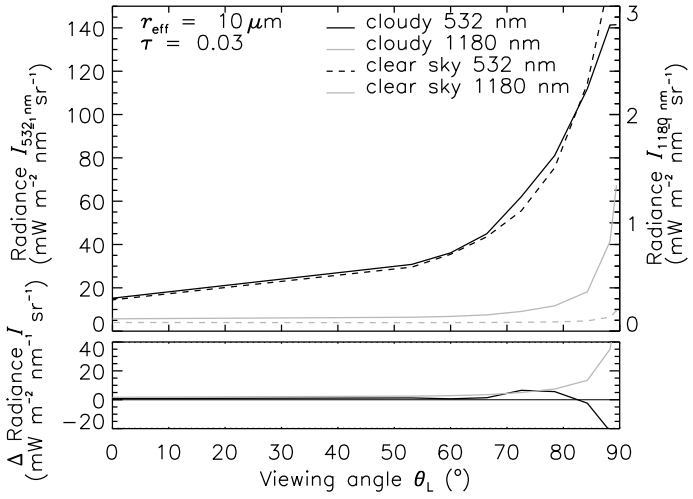

Figure 2. Simulated upward radiance I_{RT} at λ = 532 nm and λ = 1180 nm for cloudy (solid line) and clear sky (dashed line) as a function of the viewing angle θ_L. In the lower plot
between cloud and clear sky atmosphere is shown.

2.1 Wavelength sensitivity

For passive remote sensing using solar radiation, measurements at wavelengths sensitive to scattering and absorption by water droplets and ice crystals are selected. Wavelengths less than λ = 900 nm are applied to retrieve τ from nadir remote sensing. However, due to the increased photon path length of radiation reflected into any viewing angle off the nadir observation, absorption and scattering by atmospheric molecules becomes more pronounced. Figure 2 presents simulated upward I_{RT} reflected by an optically thin cirrus with $\tau = 0.03$ and $r_{eff} = 10\,\mu$m, as well as clear sky radiance for different sensor viewing angles. RTS for two wavelengths, λ = 532 nm and λ = 1180 nm, are carried out. To easily distinguish the different geometries, simulated I in nadir geometry is denoted with I^N_{RT}, while all geometries deviating from nadir are referred to off-nadir geometry and are indicated by I^L_{RT}. The sensitivity is measured by ε_τ defined as:

$$\varepsilon_\tau = \frac{dI}{d\tau} \tag{1}$$

For illustrating the impact of the cirrus on reflected I_{RT}, the difference of I_{RT} for the cloudy (solid line) and clear sky (dashed line) is shown. In general, I^L_{RT} increases with increasing θ_L due to the longer LOS. For a wavelength $\lambda = 532$ nm, no difference between cloudy and clear sky conditions is discernible for all viewing angles, because Rayleigh scattering by molecules dominates and exceeds the scattering by thin cirrus. Therefore, at λ = 532 nm cirrus can not be detected. Conversely, for λ = 1180 nm clear separation between the simulations with and without cirrus at large viewing angles for $\theta_L > 70°$ is present

Atmos. Chem. Phys. Discuss., doi:10.5194/acp-2016-970, 2016
Manuscript under review for journal Atmos. Chem. Phys.
Published: 4 November 2016

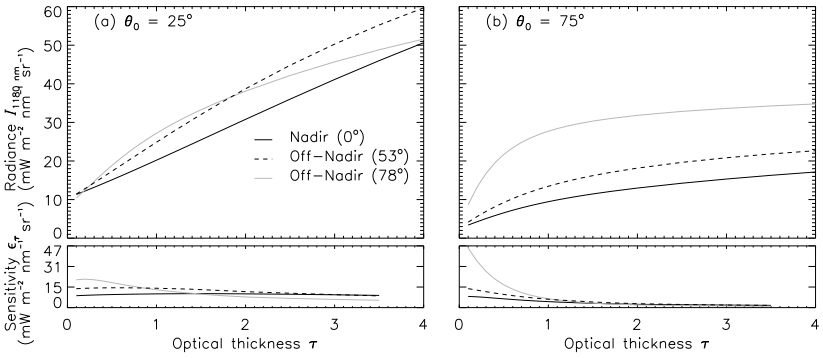

Figure 3. Simulated radiance $I_{\mathrm{RT},1180}$ for three different sensor orientations as a function of cirrus optical thickness τ. Results for solar zenith angles of $\theta_0 = 25°$ (a) and $\theta_0 = 75°$ (b) are displayed. The sensitivity ε_τ is given in the lower panels.

because the reflected $I^{\mathrm{L}}_{\mathrm{RT}}$ is increased due to larger LOS. At λ = 1180 nm wavelength Rayleigh scattering is comparable weak and does not significantly contribute to the reflected radiation. In nadir direction, a detection of cirrus is not possible due to low τ, and the overwhelming backscattering from the ground.

The RTS suggest that off-nadir observations for the detection of SVC and cirrus at near infrared wavelengths ($\lambda > 900$ nm) are more suitable.

2.2 Optical thickness and viewing angle

In general, back-scattered radiation by clouds increases with increasing τ. This sensitivity (see Eq. (1)) is the basis of most retrieval algorithms of cloud optical properties. To quantify how ε_τ is effected by θ_{L} of the sensor, RTS are performed for a set of different θ_{L} ranging between $\theta_{\mathrm{L}} = 0°$ (nadir) and $\theta_{\mathrm{L}} = 90°$ (off-nadir). Cirrus optical thickness is varied in the range of τ = 0.03 - 4 covering various kinds of cirrus clouds.

Figure 3 displays simulated $I_{\mathrm{RT},1180}$ at λ = 1180 nm wavelength for two different $\theta_0 = 25°$ (a) and $\theta_0 = 75°$ (b) as a function of τ. For each scenario, ε_τ is calculated and given in the lower panels of Fig. 3. Simulations for nadir geometry are represented by solid black lines. Results for off-nadir sensor orientations are shown by dashed ($\theta_{\mathrm{L}} = 53°$) and gray ($\theta_{\mathrm{L}} = 78°$) lines. All scenarios show an increase of $I^{\mathrm{L}}_{\mathrm{RT}}$ for increasing τ, which results from enhanced reflection.

Due to the apparent longer LOS for both θ_0, off-nadir sensor orientations yield larger ε_τ of simulated $I^{\mathrm{L}}_{\mathrm{RT}}$ as compared to the nadir geometry. The almost linear increase of the nadir radiance $I^{\mathrm{N}}_{\mathrm{RT}}$ indicates a constant ε_τ in the range of investigated τ and θ_0 presented here.

In contrast, ε_τ for off-nadir simulations change with τ and θ_0 as indicated by Fig. 3 (a) ($\theta_0 = 25°$) and Fig. 3 (b) ($\theta_0 = 75°$). For low τ and a high sun, the highest ε_τ is given for the off-nadir geometry ($\theta_{\mathrm{L}} = 78°$). A similar pattern emerges for low Sun ($\theta_0 = 75°$) resulting in larger ε_τ and a steep decrease for increasing τ. It shows that ε_τ decreases with τ and for $\tau < 3$ drops below ε_τ of nadir measurements for $\tau > 3$. The sensitivity of I with respect to τ can also be interpreted in terms of the

Atmos. Chem. Phys. Discuss., doi:10.5194/acp-2016-970, 2016
Manuscript under review for journal Atmos. Chem. Phys.
Published: 4 November 2016

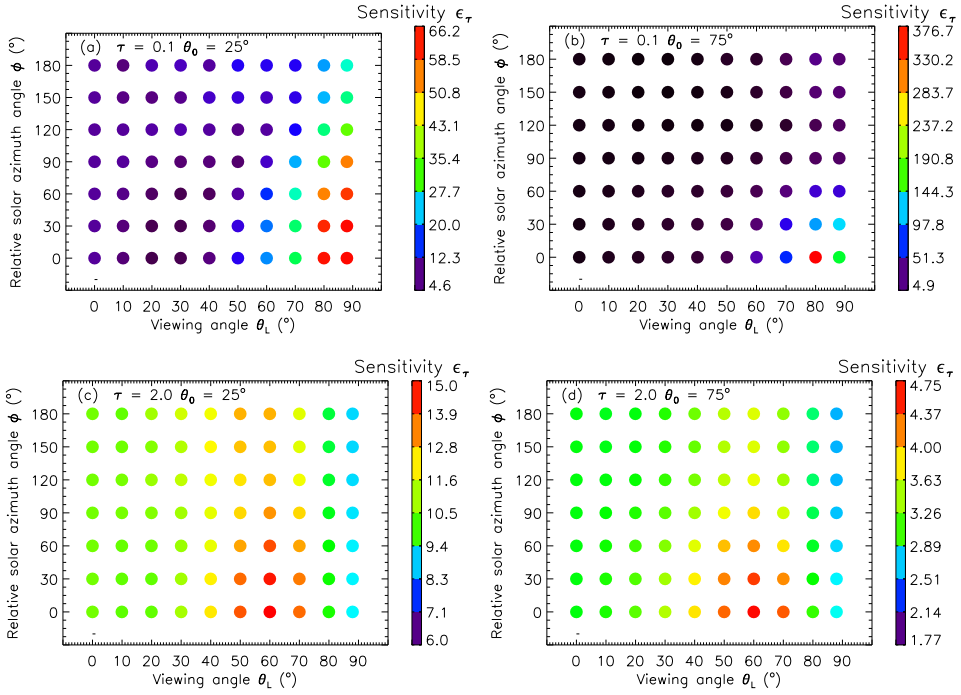

Figure 4. Sensitivity ε_τ at 1180 nm in units of $\mathrm{mW\,m^{-2}\,sr^{-1}}$ as a function of viewing angle θ_L and relative solar azimuth angle ϕ for cirrus optical thickness τ and solar zenith angle θ_0. Panel (a) for $\tau = 0.1$, $\theta_0 = 25°$, Panel (b) for $\tau = 0.1$, $\theta_0 = 75°$, Panel (c) for $\tau = 2$, $\theta_0 = 25°$ in (c) and Panel (d) for $\tau = 2$, $\theta_0 = 75°$. Different scales of the plots have to be considered.

uncertainty of retrieved τ related to an initial uncertainty in measured I. A high ε_τ leads to small retrieval uncertainties and vice versa.

In a second step, the influence of ϕ is investigated on I^L_RT in respective simulations. Figure 4 shows ε_τ for a wide range of θ_L between 0° and 90° and ϕ between 0° and 180° for two clouds of fixed cirrus optical thickness of $\tau = 0.1$ and $\tau = 2$ and two different SZA of $\theta_0 = 25°$ and $\theta_0 = 75°$. The color code in Fig. 4 represents ε_τ in units of $\mathrm{mW\,m^{-2}\,nm^{-1}\,sr^{-1}}$.

For $\tau = 0.1$ and $\theta_0 = 25°$ (Fig. 4 (a)), ε_τ ranges between 5 and 66 $\mathrm{mW\,m^{-2}\,nm^{-1}\,sr^{-1}}$. For the optically thin cirrus ε_τ is insensitive to observation geometry for $\theta_\mathrm{L} < 60°$ and all ϕ. For larger θ_L (off-nadir observations) ε_τ increases significantly reaching the maximum for $\theta_\mathrm{L} = 90°$ and $\phi = 0°$.

A similar pattern is derived for simulations assuming a lower Sun ($\theta_0 = 75°$) as shown in Fig. 4 (b). Compared to $\theta_0 = 25°$ the increase of ε_τ for $\theta_\mathrm{L} = 90°$ and $\phi = 0°$ is stronger reaching values of 377 $\mathrm{mW\,m^{-2}\,nm^{-1}\,sr^{-1}}$ while for all other geometries ε_τ almost remains constant at the same magnitude. Additionally, the maximum ε_τ is more concentrated on a single combination of θ_L and ϕ. Therefore, measurements in the range of these angles are recommended to achieve high values ε_τ for reasonable retrievals of τ.

Figure 4 (c) shows the simulated ε_τ for clouds of $\tau = 2$, $\theta_0 = 25°$ and a wide range of geometries. Compared to the optically

Atmos. Chem. Phys. Discuss., doi:10.5194/acp-2016-970, 2016
Manuscript under review for journal Atmos. Chem. Phys.
Published: 4 November 2016

Atmospheric Chemistry and Physics Discussions

thin cirrus, for optical thick cirrus the maximum of ε_τ is reduced not exceeding a value of 15 $\mathrm{mW\,m^{-2}\,nm^{-1}\,sr^{-1}}$ and shifted to smaller θ_0. While off-nadir measurements are predicted to become saturated for thin clouds, for lower optical thickness the optimal viewing angle is about $\theta_\mathrm{L} = 60°$ with the largest ε_τ occurring for ϕ between 0° and 60°. Respective simulations for $\tau = 2$, $\theta_0 = 75°$ (low Sun) are presented in Fig. 4 (d). Here the maximum of ε_τ is small with 5 $\mathrm{mW\,m^{-2}\,nm^{-1}\,sr^{-1}}$ compared to all other simulations varying τ and θ_0. Compared to simulations presented in Fig. 4 (c), the area with maximum ε_τ is concentrated between $\phi = 0°$ and $\phi = 30°$.

The RTS show that the choice of the best viewing geometry (nadir or off-nadir observations) strongly depends on τ. In order to probe a large range of cirrus with sufficient large retrieval sensitivity, measurements in different viewing directions, at least in nadir and off-nadir direction are recommended. The strong angular dependence of off-nadir measurements for viewing angles $\theta_\mathrm{L} = 90°$ requires a careful alignment of the telescope orientation in order to avoid spurious results.

2.3 Influence of surface albedo

The influence of α on the retrieval of cloud optical properties derived by passive remote sensing using the Moderate-resolution imaging spectroradiometer (MODIS) was investigated by Rolland and Liou (2001). They showed that especially retrievals of clouds with $\tau < 0.5$ are strongly influenced by variations in α. Based on RTS, Fricke et al. (2014) concluded that I^N measured in nadir direction strongly depends on the underlying surface reflectivity and that uncertainties in assumed α may cause errors of up to 50 % in the retrieval of τ.

In order to quantify and compare the influence of α on I measured in different viewing angles and nadir directions, RTS are performed. To cover the natural variability of surfaces ranging from ocean surface to ice-covered regions, α is varied between $\alpha = 0.1$ and $\alpha = 0.9$. Fig. 5 shows simulated $I^\mathrm{L}_\mathrm{RT,1180}$ at λ = 1180 nm wavelength for two clouds with $\tau = 0.1$ and $\tau = 2$ and both observation geometries.

In general, the reflected I increases with increasing α. The stronger the increase, the stronger the measurements are effected by α.

For both observation geometries, the steepest derivative

$$\gamma = \frac{\mathrm{d}I}{\mathrm{d}\alpha} \tag{2}$$

is obtained for the thin cirrus with $\tau = 0.1$. In general for increasing optically thick clouds, α becomes less important for I compared to cirrus clouds with lower τ. To quantify the impact of changes in α, the relative difference between I_RT simulated for $\alpha = 0.1$ and $\alpha = 0.9$ is calculated for each case and presented in Table 1. Maximum differences of up to 84 % are noticeable in nadir geometry for clouds of $\tau = 0.1$. Optically thick clouds show lower dependencies on α due to the increased contribution of radiation reflected by the cirrus. Comparing nadir and off-nadir geometries, the simulations show a smaller γ for off-nadir observations. The relative differences of I^L_RT for $\tau = 2$ between $\alpha = 0.1$ and $\alpha = 0.9$ is reduced to 14 %. This indicates that I measured in off-nadir geometry is less influenced by changes in α (e.g., Oikarinen (2002)). This difference in I is most pronounced for optically thin clouds where the surface contribution to measured I is large. Under unknown or variable surface

Atmos. Chem. Phys. Discuss., doi:10.5194/acp-2016-970, 2016
Manuscript under review for journal Atmos. Chem. Phys.
Published: 4 November 2016

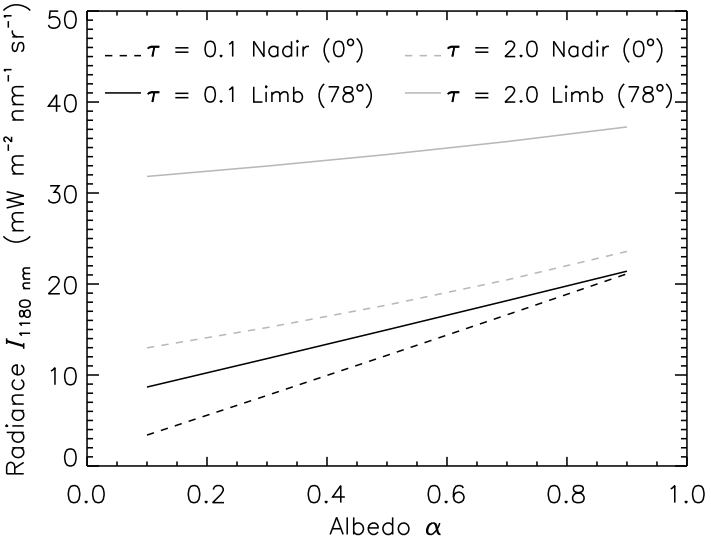

Figure 5. Influence of the surface albedo α on the measured upward radiance $I^{L}_{RT,1180}$ at λ = 1180 nm as a function of cirrus optical thickness τ and sensor orientation θ_L.

Table 1. Relative difference in $I_{RT,1180\ nm}$ for surface albedo $\alpha = 0.1$ and $\alpha = 0.9$ for different viewing angles θ_L and optical thickness τ.

	cirrus optical thickness		
viewing angle	$\tau = 0.1$	$\tau = 0.5$	$\tau = 2$
$\theta_L = 0°$	84 %	69 %	44 %
$\theta_L = 78°$	58 %	29 %	14 %

albedo conditions, observations in off-nadir direction are favoured over those in nadir direction when retrieving the optical properties of thin cirrus.

2.4 Crystal shape sensitivity

By changing the ice crystal shape in the RTS (similar cloud as described above), the sensitivity of radiance observation with respect to the ice crystal scattering phase function is investigated and compared for different viewing geometries. Ice crystals with shapes of columns, droxtals and plates are chosen and implemented in the simulations to cover the natural variability of cirrus based on the ice crystal single scattering properties provided by Yang et al. (2013). Most cirrus are composed of a mixture of ice crystal shapes (Pruppacher and Klett, 1997). Particle shape dependent scattering effects are lower due to smoothing over different crystal shapes. Therefore, an ice crystal mixture as given by Baum et al. (2005) is included in the simulations and

Atmos. Chem. Phys. Discuss., doi:10.5194/acp-2016-970, 2016
Manuscript under review for journal Atmos. Chem. Phys.
Published: 4 November 2016

Atmospheric Chemistry and Physics Discussions

serves as a reference. This is denoted with the acronym 'GHM' furtheron. The simulated $I^{\mathrm{L}}_{\mathrm{RT},1180}$ as a function of θ_{L} is presented in Fig. 6.

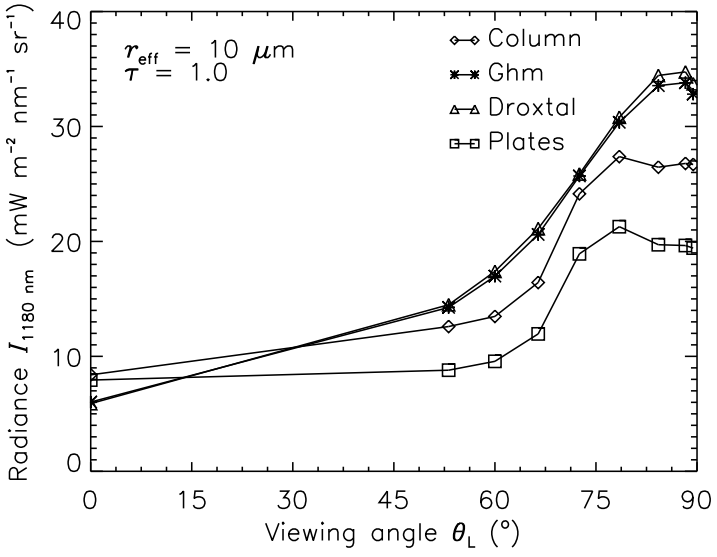

Figure 6. Simulated radiance $I^{\mathrm{L}}_{\mathrm{RT},1180}$ at λ = 1180 nm wavelength for different ice crystal shapes as a function of the viewing angle θ_{L} of the sensor.

The increase of $I^{\mathrm{L}}_{\mathrm{RT},1180}$ with increasing θ_{L} is significantly influenced by the ice crystal shape. In the simulated cases, droxtals and the GHM ice crystal mixture show a larger increase of $I^{\mathrm{L}}_{\mathrm{RT},1180}$ with increasing θ_{L} than columns and plates. While in nadir geometry ($\theta_{\mathrm{L}} = 0°$), columns and plates have a higher $I^{\mathrm{L}}_{\mathrm{RT},1180}$ than droxtals and GHM, $I^{\mathrm{L}}_{\mathrm{RT},1180}$ measured at viewing angles $\theta_{\mathrm{L}} > 50°$ is higher for droxtals and the GHM crystal mixture. The spatial distribution obtained for droxtals results from the enhanced forward and reduced sideways scattering compared to other crystal shapes.

For simulations in nadir direction the relative difference between lowest (droxtals) and highest (columns) $I^{\mathrm{N}}_{\mathrm{RT},1180}$ differs by up to $41.5\,\%$ of the absolute radiance of $6.1\,\mathrm{mW\,m^{-2}\,nm^{-1}\,sr^{-1}}$ obtained the 'GHM' crystal mixture.

For off-nadir observations the relative and absolute change in $I^{\mathrm{L}}_{\mathrm{RT},1180}$ is even larger between $\theta_{\mathrm{L}} = 60°$ and $\theta_{\mathrm{L}} = 90°$. With increasing θ_{L} the differences of $I^{\mathrm{L}}_{\mathrm{RT},1180}$ increase up to a maximum of 43.5% at $\theta_{\mathrm{L}} = 78°$ between droxtals and plates with respect to the absolute value of $33.8\,\mathrm{mW\,m^{-2}\,nm^{-1}\,sr^{-1}}$ for GHM.

The simulations show that the relative change in simulated $I^{\mathrm{L}}_{\mathrm{RT},1180}$ due to ice crystal shape effects increases with θ_{L}. Therefore, for cirrus of low τ the interpretation of off-nadir observations rely even stronger on a correct assumption of ice crystal shape than nadir observations. Multiangular observations covering the angular pattern (Fig. 6), may provide sufficient information to retrieve ice crystal shape as proposed by Schäfer et al. (2013).

Atmos. Chem. Phys. Discuss., doi:10.5194/acp-2016-970, 2016
Manuscript under review for journal Atmos. Chem. Phys.
Published: 4 November 2016

Atmospheric Chemistry and Physics Discussions

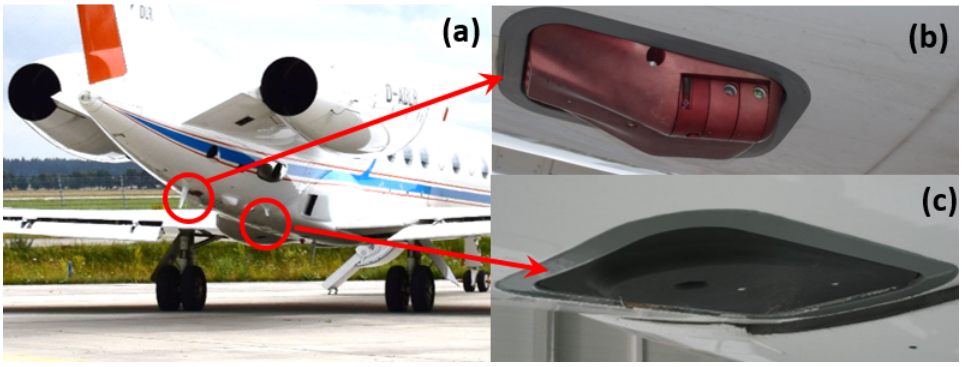

Figure 7. Optical inlets of mini-DOAS (b) and SMART (c) mounted at the lower aircraft fuselage.

3 Airborne measurements

Simultaneous airborne measurements of I in nadir and off-nadir geometry were conducted during four campaigns using the HALO research aircraft. During NARVAL shallow convection in the North Atlantic trade-wind region of the northern Atlantic (NARVAL South, December 2013) and cloud systems associated with the North Atlantic mid-latitude stormtrack (NARVAL North, January 2014) were probed (Klepp et al., 2014). During the ML-CIRRUS campaign natural and contrail cirrus in the mid-latitudes was investigated in March and April 2014 (Voigt et al., 2016). Deep convective clouds were observed during the Aerosol, Cloud, Precipitation, and Radiation Interactions and Dynamics of Convective Cloud Systems (ACRIDICON-CHHUVA) mission in September 2015 (Wendisch et al., 2016).

During these missions, a suite of different active and passive remote sensing instruments was operated on board HALO, including passive solar radiance measurements by SMART and the mini-DOAS. While SMART measured radiometrically calibrated radiance I_S^N in nadir direction, the mini-DOAS instrument simultaneously measures in nadir and varying viewing directions in ultra-violet (UV)/ visible (VIS)/ near-infrared (IR) wavelength ranges. The mini-DOAS measurements are traditionally analyzed by applying the Differential optical absorption spectroscopy (DOAS) technique. DOAS relies on an analysis of intensity ratios of two spectroscopic observations made under largely different atmospheric conditions. By exploiting ratios of I, DOAS measurements are inherently radiometrically calibrated in a relative but not absolute sense. Therefore no absolute radiometric calibration for I for the mini-DOAS is available. In addition to the two passive sensors, active lidar measurements with the Water Vapor Lidar Experiment in Space (WALES) were performed during NARVAL and ML-CIRRUS.

In Fig. 7 (a) the position of the apertures at the aircraft fuselage is indicated. The optical inlets of mini-DOAS and SMART for upward radiation are shown in Fig. 7 (b) and Fig. 7 (c) respectively.

3.1 The SMART instrument

Depending on the configuration, SMART measures spectral upward $F_{S,\lambda}^{\uparrow}S$ and downward irradiance $F_{S,\lambda}^{\downarrow}$, as well as upward radiance I_S^N (Wendisch et al., 2001, 2016). In this paper the focus is on I_S^N measurements which are available for the four

Atmos. Chem. Phys. Discuss., doi:10.5194/acp-2016-970, 2016
Manuscript under review for journal Atmos. Chem. Phys.
Published: 4 November 2016

Atmospheric Chemistry and Physics Discussions

Table 2. Individual sources of uncertainty and total uncertainties for the upward radiance $I^{N}_{S,1180}$ at a wavelength of λ = 1180 nm

.

	Source of Uncertainty	$\lambda = 1180\,\mathrm{nm}$
$I^{N}_{S,1180}$	Spectral Calibration	$< 1\,\%$
	Radiometric Calibration	$8.5\,\%$
	Signal-to-Noise-Ratio	$11.6\,\%$
	Transfer Calibration	$< 1.1\,\%$
	Total	$14.5\,\%$

HALO missions introduced above.

To cover almost the entire solar spectral range, SMART measures I^{N}_{S} with two separate spectrometers, one for the visible and near-infrared (VNIR) range from λ = 300 nm to λ = 1000 nm and a second one sampling the shortwave infrared (SWIR) range from λ = 900 nm to λ = 2200 nm. Merging the spectra, about $97\,\%$ of the solar spectrum is covered (Bierwirth et al., 2009). The spectral resolution defined by the full width at half maximum (FWHM) is 8 - 10 nm for the SWIR spectrometer and 2 - 3 nm for the VNIR spectrometer.

The radiance optical inlet of SMART has an opening angle of $\Delta = 2^{\circ}$ and a sampling time of 0.5 s. Considering aircraft groundspeed and the distance of 500 m between the cloud and the aircraft the resulting footprint is about 18 x 110 m for an individual I^{N}_{S} measurement. For a distance of 1000 m between sensor and cloud the footprint increases to 35 x 220 m.

Prior to each campaign SMART was radiometrically calibrated in the laboratory using certified calibration standards traceable to NIST and by secondary calibration using a travelling standard during the operation on HALO. The total measurement uncertainty of I^{N}_{S} is about $5.4\,\%$ for the VNIR and $14.5\,\%$ for the SWIR range which consist of individual errors due to the spectral calibration, the spectrometer noise and dark current, the radiometric calibration and the transfer calibration (Brückner et al., 2014). In Table 2 the contributions of each individual source of uncertainty is given for measurements at λ = 1180 nm wavelength. The main uncertainty results from the Signal-to-Noise-Ratio (SNR) and the calibration standard, while spectral and transfer calibration errors are almost negligible. Averaging a time series of measurements will reduce the contribution of sensor noise to the signal.

3.2 The mini-DOAS instrument

The mini-DOAS is a passive airborne remote sensing system originally designed to retrieve vertical profiles of trace gases, aerosol and cloud particles. The analyzis is based on the Differential Optical Absorption Spectroscopy (DOAS) technique that applies least square retrievals on the spectral shape of the observed I^{L}_{mD} (Platt and Stutz, 2008). Spectral absorption bands of molecules and particles are measured at moderate spectral resolution (FWHM 0.1 nm) to quantify the absorption of solar radiation by trace gases along the light path. DOAS measurements are primarily used to estimate trace gas concentrations and associated photochemistry in the atmosphere. Here, measured I^{L}_{mD} are employed for the remote sensing of clouds.

Atmos. Chem. Phys. Discuss., doi:10.5194/acp-2016-970, 2016
Manuscript under review for journal Atmos. Chem. Phys.
Published: 4 November 2016

Atmospheric Chemistry and Physics Discussions

The mini-DOAS is designed as a compact, lightweight and robust system to be operated aboard the HALO aircraft. The instrument consists of six telescopes which are connected via fiber bundles to six optical spectrometers. One set of the optical inlets is fixed in nadir configuration while the other telescopes can be tilted between $\theta_L = 0°$ and $\theta_L = 90°$. Two sets of three different spectrometers are applied to cover the ultraviolet (UV) spectral range from 310 nm to 440 nm (FWHM 0.5 nm), the visible (VIS) range from 420 nm to 650 nm (FWHM 1 nm) and the near infrared (SWIR) range from 1100 nm to 1680 nm (FWHM 5 nm). In the UV and VIS range Charged-Coupled Devices (CCD) sensors are used as detectors. The detection in the SWIR range is performed by Photo Diode Arrays (PDA).

The telescopes are mounted on an aperture plate at the lower side of the aircraft fuselage. The scanning telescopes have rectangular fields of view of about $0.6°$ in vertical direction and $3°$ in horizontal direction. During scanning measurements the telescopes are directed to the starboard side of the aircraft. Changes of aircraft roll angles are compensated within $0.1°$. The orientation of the nadir telescope is kept fix with respect to the aircraft major axis. Therefore no compensation of the aircraft roll angle is performed.

The evacuated spectrometer housing is immersed into an isolated water / ice tank to ensure a constant temperature and pressure of the spectrometers independent from changing outside conditions. Evacuation of the housing and temperature stabilization is necessary to guarantee a stable optical imaging, which is indispensable for DOAS applications. A spectral calibration of the spectrometers assures that wavelength shifts are less than 0.05 nm.

3.3 The WALES instrument

The Water Vapor Lidar Experiment in Space Demonstrator (WALES) is an airborne Differential Absorption Lidar (DIAL) with additional aerosol and cloud detection capabilities operated on the German research aircraft Falcon and HALO (Wirth et al., 2009).

For particle detection WALES has two backscatter and depolarization channels at λ = 532 nm and λ = 1064 nm wavelength and an additional high spectral resolution lidar (HSRL) channel at λ = 532 nm (Esselborn et al., 2008). The HSRL channel allows the retrieval of the backscatter coefficient of clouds at λ = 532 nm without assumptions about the phase function of the cloud particles. Also the apparent transmission of the cloud can easily be determined from the HSRL-channel. If multiple scattering effects are neglected this apparent transmission is simply the exponential of the negative optical thickness.

Unfortunately, larger cirrus particles usually show a pronounced forward scattering peak, which may contain a significant fraction of the scattered energy. This may lead to an underestimation of τ calculated from the individual particle extinction cross sections (see e.g. (Platt, 1981)). The optical thickness data presented in this paper are corrected for the forward scattering effect following the algorithm proposed by Eloranta (1998). To apply this correction scheme, an effective particle radius is assumed, which determines the width of the forward scattering peak. Best compensation of the multiple scattering decay below the cloud was found for $r_{\mathrm{eff}} = 35 \pm 5\,\mu\mathrm{m}$ in good agreement with the climatological values proposed by Bozzo et al. (2008). The mean correction factor for the data set shown in this paper was 7%.

Atmos. Chem. Phys. Discuss., doi:10.5194/acp-2016-970, 2016
Manuscript under review for journal Atmos. Chem. Phys.
Published: 4 November 2016

Atmospheric Chemistry and Physics Discussions

4 Cross-calibration

Since no radiometric calibration is available for mini-DOAS, simultaneous measurements of SMART and mini-DOAS are used to cross-calibrate both instruments. The cross-calibration relies on the radiometric calibration of SMART and allows to derive calibrated I_{mD} from mini-DOAS measurements. Flight sections with inhomogeneous α and various cloud conditions are selected to obtain a calibration valid for a wide range of different I. Such conditions were present during the ML-CIRRUS flight on the 26 March 2014 including measurements over southern Germany, Belgium, United Kingdom, Ireland and the northern Atlantic Ocean westerly of Ireland. The cross-calibration is performed for nadir and off-nadir viewing geometries of mini-DOAS. The results are presented for two wavelengths at λ = 1180 nm and λ = 1600 nm which are frequently used in cloud retrievals. Different FWHM of both spectrometer systems are considered by convoluting the spectrally higher resolved measurements of the mini-DOAS with the corresponding FWHM of the SMART spectrometer (8-19 nm).

4.1 Nadir radiance

The nadir sensors of the mini-DOAS operate in fixed position, thus providing a large data set of simultaneous measurements with SMART. The time stamps of both instruments are corrected for temporal offsets in the data acquisition. Scatter plots of $I^{\mathrm{N}}_{\mathrm{S},\lambda}$ and mini-DOAS raw data are shown in Fig. 8 for both wavelengths. For each data point a linear regression after Theil (1992) and Sen (1968) is performed. Using the method after Theil and Sen the influence of outliers on the regression is reduced and the linear calibration equation $I^{\mathrm{N}}_{\mathrm{S},\lambda} = a_0 \cdot N^{\mathrm{N}}_{\mathrm{mD},\lambda} + a_1$ for the mini-DOAS radiances are determined. $I^{\mathrm{N}}_{\mathrm{S},\lambda}$ is the radiance measured by SMART, $N^{\mathrm{N}}_{\mathrm{mD},\lambda}$ the raw signal of mini-DOAS and a_0 and a_1 the calibration coefficients. The linear regressions are indicated by the gray lines in Fig. 8 (a) and Fig. 8 (c). For the ML-CIRRUS flight on 26 March 2014 the nadir geometry calibration coefficients are determined as $a_0 = 0.31\,\mathrm{mW\,m^{-2}\,sr^{-1}}$ and $a_1 = 0.55\,\mathrm{mW\,m^{-2}\,sr^{-1}}$ for λ = 1180 nm with an uncertainty of $\pm 0.24\,\mathrm{mW\,m^{-2}\,sr^{-1}}$. Similar calibrations are performed for flights during the NARVAL and ACRIDICON-CHUVA campaigns. All calibration coefficients are summarized in Table 3. The coefficients depend on various environmental condition where the temperature dependence of the mini-DOAS spectrometers is the most influencing parameter.

The uncertainty is mostly related to differences of the FOV and the related difference in the observed scene and possible minor mismatches of the nadir orientation of both sensors. This means that both sensors do not always observe the exact same cloud area. For the λ = 1600 nm wavelength, a_0 is higher compared to λ = 1180 nm in all analyzed flights indicating the different spectral sensitivities of both sensors with SMART in comparison with mini-DOAS beeing more sensitive at λ = 1600 nm than at λ = 1180 nm wavelength.

The derived cross-calibrations of mini-DOAS are applied to all mini-DOAS measurements. A measurement example of a time series of calibrated mini-DOAS radiances I_{mD} is shown in Fig. 8 (b) and 8 (d) for a 18 minute flight section measured on the 26 March 2014.

The radiance time series for λ = 1180 nm of both sensors agree within the SMART error range for most data points, except for some radiance peaks. These differences likely result from the different FOV of both instruments and the presence of patches of low cumulus with high reflectivity. A similar result is obtained for λ = 1600 nm. The differences of the mean

Atmos. Chem. Phys. Discuss., doi:10.5194/acp-2016-970, 2016
Manuscript under review for journal Atmos. Chem. Phys.
Published: 4 November 2016

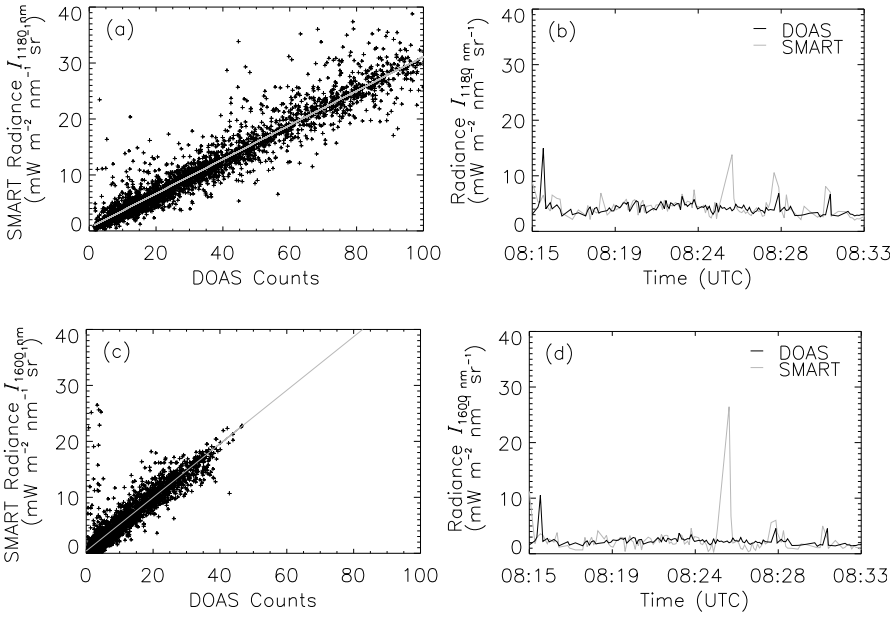

Figure 8. Panel (a) and (c) show comparisons of SMART radiance I_S^N and mini-DOAS raw signal for nadir channels at λ = 1180 nm and λ = 1600 nm wavelength. Panel (b) and (d) show time series of measured SMART radiance $I_{S,\lambda}^N$ and calibrated mini-DOAS radiance $I_{mD,\lambda}^L$ for the ML-CIRRUS flight on 26 March 2014.

radiance between both instruments for the time period presented in Fig. 8 is $0.75\,\mathrm{mW\,m^{-2}\,nm^{-1}\,sr^{-1}}$ at λ = 1180 nm and $0.5\,\mathrm{mW\,m^{-2}\,nm^{-1}\,sr^{-1}}$ at λ = 1600 nm.

4.2 Off-nadir radiance

The scanning telescopes of the mini-DOAS typically run in a sequential mode scanning different θ_L. During selected flight segments the scanning sequences are configured to include nadir measurements. Due to this sequential mode less measurements from the off-nadir channels are available for cross-calibration with SMART because only measurements in nadir sensor orientation are applicable for the cross-calibration. To ensure a statistically sufficient number of samples, the entire flight of 26 March 2014 is analyzed applying the same methods used for the calibration of the nadir channels. Figures 9 (a) and 9 (c) show the cross-calibration of SMART radiances $I_{S,\lambda}^N$ and mini-DOAS raw data $N_{mD,\lambda}^L$ and the linear fit (gray line) used for calibration. For the s near infrared scanning channels the calibration coefficients are determined as $a_0 = 0.31\,\mathrm{mW\,m^{-2}\,sr^{-1}}$ with no offset a_1 for λ = 1180 nm and an uncertainty of $\pm 0.2\,\mathrm{mW\,m^{-2}\,sr^{-1}}$. Similar to the nadir channels, the calibration coefficients for the the off-nadir channel at λ = 1600 nm wavelength with $a_0 = 0.47$ are higher compared to the λ = 1180 nm wavelength.

The calibration of the off-nadir channels is repeated for the NARVAL flights while for all ACRIDICON-CHUVA flights no

Atmos. Chem. Phys. Discuss., doi:10.5194/acp-2016-970, 2016
Manuscript under review for journal Atmos. Chem. Phys.
Published: 4 November 2016

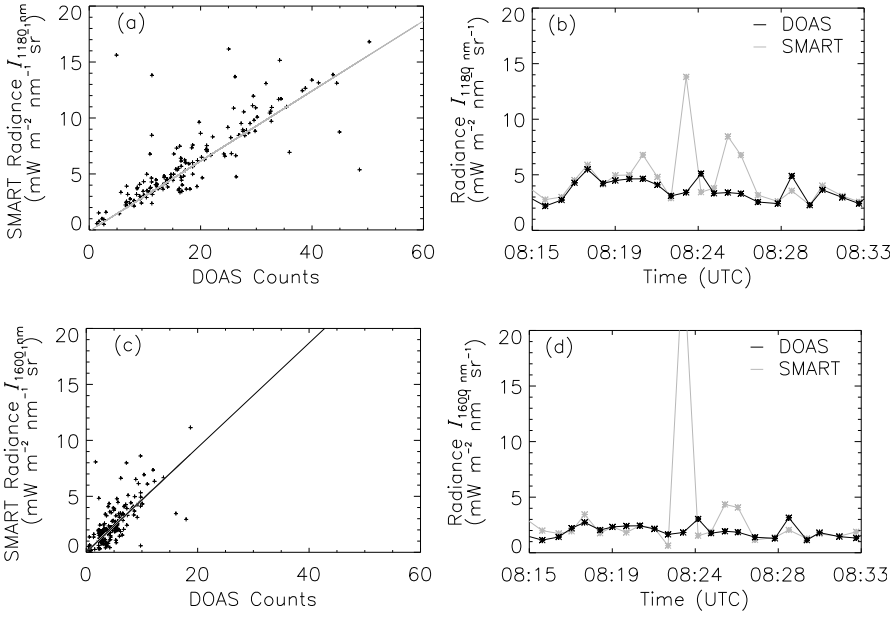

Figure 9. Panel (a) and (c) show a comparison of SMART radiance $I^{N}_{S,\lambda}$ and mini-DOAS raw signal $N^{L}_{mD,\lambda}$ for the scanning channels at λ = 1180 nm and λ = 1600 nm wavelength. Panel (b) and (d) show time series of measured SMART radiance $I^{N}_{S,\lambda}$ and calibrated mini-DOAS radiance $I^{L}_{mD,\lambda}$ for the ML-CIRRUS flight on 26 March 2014.

nadir observations of the off-nadir channels are available. Table 3 provides a summary of all calibration coefficients derived for the off-nadir channels.

Similar to Fig. 8, Figures 9 (b) and 9 (d) show time series of SMART radiance $I^{N}_{S,\lambda}$ and calibrated mini-DOAS nadir observations $I^{N}_{mD,\lambda}$ for a 18 minutes flight segment of the ML-Cirrus on 26 March 2014. In general, the radiance pattern observed by SMART is represented by the calibrated mini-DOAS radiance. However, individual data points differ due to differences in FOV resulting in mean differences of $0.78\,\mathrm{mW\,m^{-2}\,nm^{-1}\,sr^{-1}}$ at 1180 nm and $0.38\,\mathrm{mW\,m^{-2}\,nm^{-1}\,sr^{-1}}$ at λ = 1600 nm which ranges below the uncertainty range of SMART.

4.3 Temporal stability of cross-calibration

The mini-DOAS instrument is designed to maintain a stable radiometric calibration but this can change from campaign to campaign. Therefore, cross-calibration coefficients for different campaigns and flights are derived to consider changes of the optical setup, for example when changing the optical fibers. Using different calibration factors for the mini-DOAS instrument as inferred for the different campaigns, Fig. 10 shows a comparison of measured I at λ = 1180 nm wavelength from a four minutes long flight segment over the Amazon region on 12 September 2014. The comparison clearly indicates that the measurements

Atmos. Chem. Phys. Discuss., doi:10.5194/acp-2016-970, 2016
Manuscript under review for journal Atmos. Chem. Phys.
Published: 4 November 2016

Atmospheric Chemistry and Physics Discussions

Table 3. Calibration coefficients a_0 and a_1 in units of $\mathrm{mW\,m^{-2}\,nm^{-1}\,sr^{-1}}$ for mini-DOAS nadir and scanning channel radiance obtained for NARVAL (19 December 2013), ML-CIRRUS (26 March 2014) and ACRIDICON-CHUVA (9, 12 and 23 September 2014).

	1180 nm				1600 nm			
	Nadir		Off-nadir		Nadir		Off-nadir	
	$(\mathrm{mW\,m^{-2}\,nm^{-1}\,sr^{-1}})$							
	a_0	a_1	a_0	a_1	a_0	a_1	a_0	a_1
NARVAL (19.12.)	0.26	5.40	0.23	0.90	0.28	1.32	0.26	0.10
ML-CIRRUS (26.03.)	0.31	0.55	0.31	0.00	0.43	0.25	0.47	0.02
ACRIDICON-CHUVA (09.09)	0.24	5.28			0.37	2.80		
ACRIDICON-CHUVA (12.09.)	0.34	0.94			0.51	0.77		
ACRIDICON-CHUVA (23.09.)	0.31	3.43			0.40	0.59		

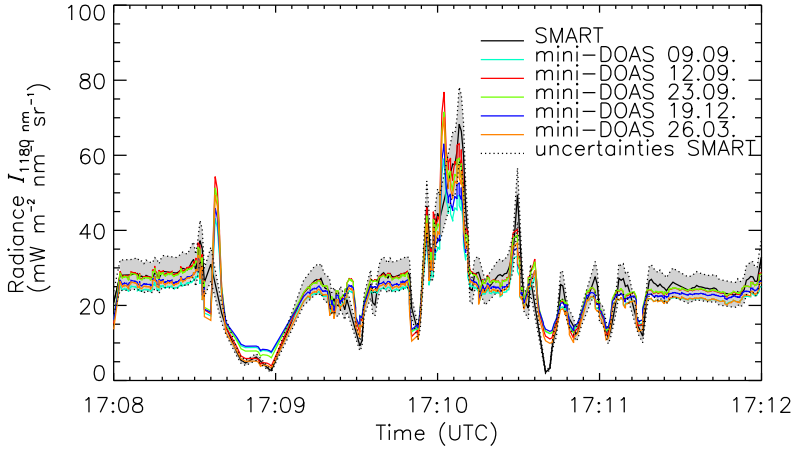

Figure 10. Time series of the nadir radiance of SMART $I^{\mathrm{N}}_{\mathrm{S},1180}$ and of the mini-DOAS $I^{\mathrm{N}}_{\mathrm{mD},1180}$ nadir channel at λ = 1180 nm using different calibrations as indicated in the legend. The uncertainty range of SMART radiance is shaded gray.

of I of both sensors are not systematically biased and agree within the errors of each sensor except when differences at small spatial scales appear.

The deviation of the different calibrations is below $2.9\,\mathrm{mW\,m^{-2}\,nm^{-1}\,sr^{-1}}$ indicating a reasonable stability of the calibrations. This suggests, that the calibration coefficients do not change significantly with time and the mini-DOAS calibration is relatively constant.

Atmos. Chem. Phys. Discuss., doi:10.5194/acp-2016-970, 2016
Manuscript under review for journal Atmos. Chem. Phys.
Published: 4 November 2016

Atmospheric Chemistry and Physics Discussions

5 Retrieval of cirrus optical thickness

5.1 Iterative algorithm

By using all three calibrated radiance data sets obtained from SMART $I_{\mathrm{S}}^{\mathrm{N}}$, mini-DOAS nadir channels $I_{\mathrm{mD}}^{\mathrm{N}}$, and off-nadir channels $I_{\mathrm{mD}}^{\mathrm{L}}$, an iterative retrieval algorithm of τ is developed and applied. It is based on the bi-spectral reflectance method described by Twomey and Seton (1980), and Nakajima and King (1990). Here it was adapted for ice clouds with respect to ice crystal shape and used wavelength, e.g. by Ou et al. (1995) and Rolland et al. (2000). For retrieving τ rough aggregates are assumed using pre-calculated ice crystal parametrizations after Yang et al. (2013). The iterative algorithm utilizes the spectral reflectivity $\mathcal{R}_\lambda$ which is defined as the ratio of spectral upward I_λ to spectral downward $F_\lambda^\downarrow$,

$$\mathcal{R}_\lambda = \frac{I_\lambda \pi}{F_\lambda^\downarrow} \tag{3}$$

During ML-CIRRUS, $F_\lambda^\downarrow$ is taken from the actual SMART measurements on HALO. Measured $F_\lambda^\downarrow$ allows to identify and eliminate any influence of the radiation field above the aircraft, for example by cirrus. As an alternative to pre-calculate Look-up-Tables (LUT) by extensive forward simulations, an iterative algorithm is applied that runs RTS adjusted to each single measurement. This allows to set up simulations by actual input parameters for each measurement i. e. θ_0, ϕ, longitude, latitude and flight altitude. In that way, uncertainties caused by inaccurate assumptions in the RTS input are minimized. Additionally, the iterative method is not limited to a specific pre-calculated grid of τ and r_{eff} as used in LUTs where a certain interval of preselected τ and r_{eff} are given. The iterative algorithm automatically adjusts the range of τ and r_{eff} without interpolation until reaching the final result.

Figure 11 shows a scheme of the retrieval algorithm, which starts with an initial guess of τ_0. Using the initial guess of τ and of any other cloud parameters, the cloud reflectivity $\mathcal{R}_{\mathrm{sim}}$ is simulated and compared to the measurements $\mathcal{R}_{\mathrm{meas}}$ of SMART and mini-DOAS, respectively. The ratio between $\mathcal{R}_{\mathrm{sim,n}}$ and $\mathcal{R}_{\mathrm{meas}}$ derived for each iteration step n is used to scale the particular guess τ_{n} by

$$\tau_{\mathrm{n+1}} = \tau_{\mathrm{n}} \cdot \frac{\mathcal{R}_{\mathrm{sim}}}{\mathcal{R}_{\mathrm{meas}}}. \tag{4}$$

The adjusted optical thickness $\tau_{\mathrm{n+1}}$ is used in the RTS for the new iteration step $n+1$. The iteration of τ is repeated until the change of τ_{n} between two iteration steps is smaller than $5\,\%$ or a limit of $n > 100$ iteration steps is reached. These stop criteria determine the accuracy of the iterative retrieval. For a typical cirrus observed during ML-CIRRUS with an average τ of 0.32, the cirrus optical thickness can be retrieved with a accuracy of about $\tau \pm 0.03$.

In case of measurements of optically thin cirrus, the retrieval can be applied for τ only. For these situations the nadir radiance at λ = 1600 nm wavelength (ice absorption band) to retrieve r_{eff} is low and only measured with high uncertainty. For a cirrus cloud

Atmos. Chem. Phys. Discuss., doi:10.5194/acp-2016-970, 2016
Manuscript under review for journal Atmos. Chem. Phys.
Published: 4 November 2016

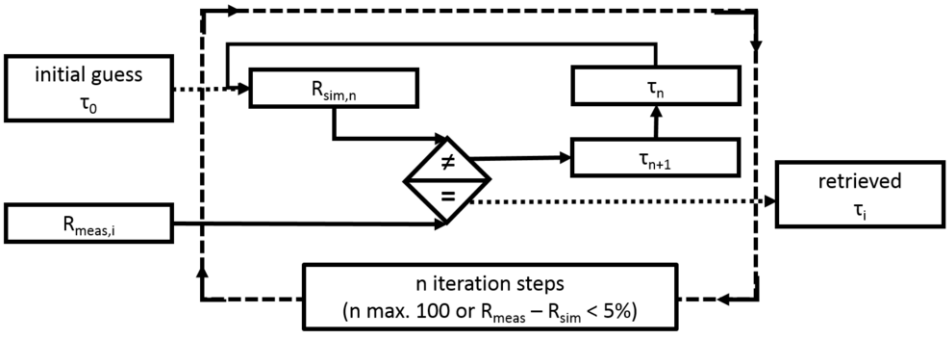

Figure 11. Scheme of the iterative algorithm. For every single measurement i an iteration loop is started with an initial guess τ_0 until measured $\mathcal{R}_{\text{meas}}$ and simulated $\mathcal{R}_{\text{sim}}$ reflectivity converge within $5\,\%$ difference or a maximum of 100 iteration steps is reached. At the end of the process the result is saved.

with $\tau = 0.03$, $I^{\text{N}}_{\text{RT},1600}$ the simulated upward I is in the range of $0.2\,\text{mW}\text{m}^{-2}\text{sr}^{-1}$. Such low I are in the range of the electronic noise of the spectrometers leading to low Signal-to-Noise-Ratio and high retrieval uncertainties. Especially for cirrus with low τ the variation of $I^{\text{N}}_{\text{RT},1600}$ with respect to changes in r_{eff} is low. Simulations show, that for $\tau = 0.5$ the difference of $I^{\text{N}}_{\text{RT},1600}$ in nadir direction is only $0.1\,\text{mW}$ when changing r_{eff} from $10\,\mu\text{m}$ to $20\,\mu\text{m}$ indicating the low sensitivity of r_{eff} retrievals at this wavelength. Therefore, a reliable retrieval of r_{eff} with reasonable accuracy is not feasible. In the retrieval algorithm r_{eff} is fixed to $30\,\mu\text{m}$ a typical value of ice crystals observed by in-situ measurements during ML-CIRRUS (Voigt et al., 2016). Therefore, the influence of an invalid assumption of r_{eff} on the iterative retrieval is analyzed. For this purpose the retrieval is tested for a typical cirrus of $\tau = 0.3$. and is run with three different assumptions of r_{eff} of $20\,\mu\text{m}$, $30\,\mu\text{m}$, $40\,\mu\text{m}$, representing the uncertainty of r_{eff}. These simulations imply that the retrieved τ changes only by ± 0.02 between smallest and largest r_{eff}, resulting in a relative error in τ of $6.7\,\%$. The uncertainty in measured $I^{\text{N}}_{\text{S},1600}$ causes a retrieval uncertainty of $\tau \pm 0.02$. This justifies the fixed choice of r_{eff} in this specific cloud case. However, the dependence of retrieved τ and the assumption of r_{eff} may vary with α, ice crystal size, τ and λ used in the retrieval.

5.2 ML-CIRRUS case study

The iterative retrieval is applied for a selected leg of the ML-CIRRUS flight on 26 March 2014. For this day the Terra MODIS image (overpass time 10:40 UTC) indicates the cloud, with a west to east gradient in τ (Fig. 12). In the figure the flight track of HALO is indicated by the blue line. The cloud retrieval is applied to the HALO flight segment for the leg between 08:15 UTC and 08:36 UTC (highlighted in red) when HALO did fly above the cirrus. During this period the aircraft flew constantly at 12.6 km height along $14°$ W. Due to low horizontal advection and hence slow cloud formation it can be expected that the Terra MODIS image (Fig. 12) actually reflects the cloud cover investigated by HALO. The cirrus developed along a warm conveyor belt and contained embedded contrails as indicated by the lidar backscatter profiles at λ = 1064 nm and λ = 532 nm of WALES (see Fig. 13). The time period for which τ is retrieved is marked by the black frame. The selected flight segment

Atmos. Chem. Phys. Discuss., doi:10.5194/acp-2016-970, 2016
Manuscript under review for journal Atmos. Chem. Phys.
Published: 4 November 2016

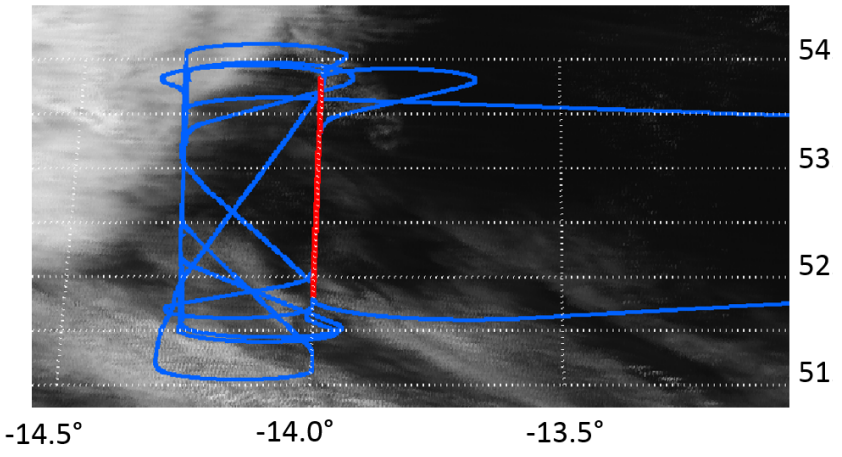

Figure 12. Investigated cloud field observed by MODIS-Terra on 26 March 2014. The flight track of HALO is indicated by the blue line. The flight leg between 08:15 UTC and 08:36 UTC for which the cirrus retrieval is performed is indicated by the red line.

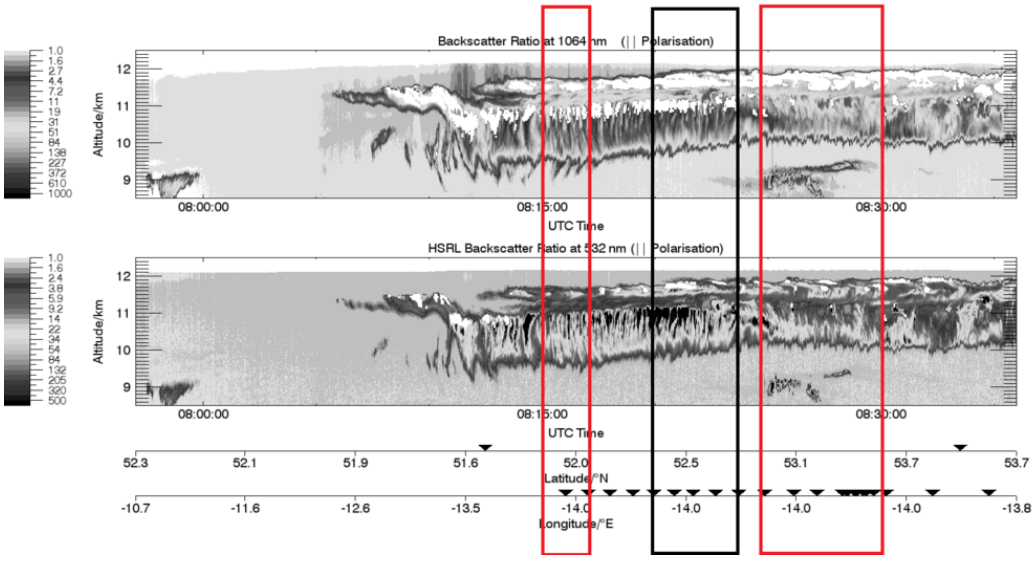

Figure 13. Vertical profiles of backscatter ratios at λ = 1064 nm (upper panel) and λ = 532 nm (lower panel) measured by WALES between 07:50 UTC and 08:50 UTC. The time period for which τ is retrieved is marked by the black rectangle. Areas which are influenced by a second cloud layer are highlighted by the red boxes.

is characterized by a constant cloud top height and a slightly increasing cloud bottom height towards northern flight direction. While the cloud top is relatively homogeneous, the lower part of the cirrus shows small-scale variability mainly connected to sedimentation of ice crystals.

Atmos. Chem. Phys. Discuss., doi:10.5194/acp-2016-970, 2016
Manuscript under review for journal Atmos. Chem. Phys.
Published: 4 November 2016

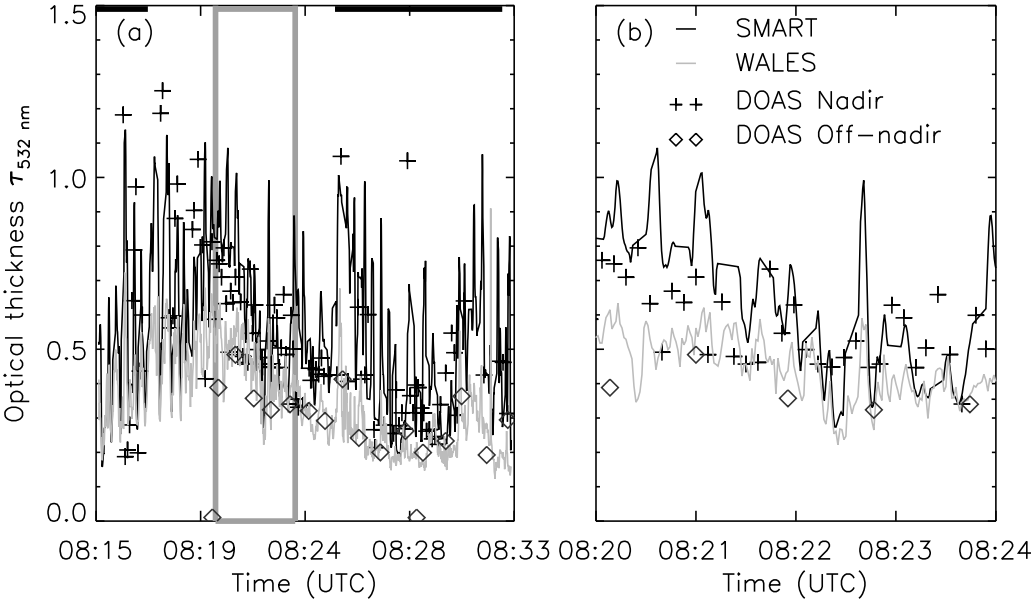

Figure 14. Time slices of the investigated flight segment on 26 March 2014 (a) and zoom (b) of τ at $\lambda = 532$ nm retrieved from SMART (black line), WALES (gray line), mini-DOAS Off-nadir (diamonds) and nadir spectrometers (crosses) along the flight track of ML-CIRRUS flight on 26 March 2014. Sections with the second cloud layer are marked by the black lines at the top of (a).

Figure 14 (a) shows a 20 minutes long flight segment of retrieved τ at $\lambda = 532$ nm calculated from SMART, mini-DOAS nadir and scanning spectrometers. WALES measurements are included for comparison. Along the analyzed cirrus, the retrieved τ ranges between 0.1 and 1.3 indicating the horizontal variability of the cirrus. The general decrease of τ towards higher latitudes (increasing time) matches with the cloud pattern observed by WALES. While SMART and mini-DOAS nadir channels resolve the cirrus variability observed by WALES, the off-nadir channel retrieval does not cover these fluctuations due to the reduced time resolution of the scanning mode and the large spatial scale (tenth of kilometers) over which off-nadir measurements average. At some locations, e. g. 08:21 UTC, τ retrieved by SMART and mini-DOAS significantly exceed the measurements of WALES. In Fig. 13 these areas are highlighted in red. The first section ranges from 08:15 UTC until 08:17 UTC. The higher reflectivity as compared to the other parts of the flight leg is caused by ice crystals falling out of the cirrus resulting in higher upward I. The second segment with higher reflectivity is likely due to an underlying cirrus between 8.5 km and 9.5 km altitude. The differences between SMART, mini-DOAS and WALES result from the detection of the second cloud layer by SMART and mini-DOAS, which is obscured for WALES. Therefore a positive systematic offset of the retrieved τ occurs. These data points are excluded from the following analysis.

For the investigated time period the retrieved average of τ at 532 nm is 0.54 (SMART), 0.49 (mini-DOAS nadir spectrometers), 0.27 (mini-DOAS scanning spectrometer) and 0.32 (WALES). The result indicate a general agreement of τ by SMART and

Atmos. Chem. Phys. Discuss., doi:10.5194/acp-2016-970, 2016
Manuscript under review for journal Atmos. Chem. Phys.
Published: 4 November 2016

Atmospheric Chemistry and Physics Discussions

mini-DOAS nadir, while lower τ are inferred from mini-DOAS off-nadir and WALES measurements. Taking the WALES measurements as a reference, the measurements of SMART and mini-DOAS overestimate τ. However, by estimating the uncertainty of the mini-DOAS and SMART basing on RTS, the measurement error of $I^{\mathrm{N}}_{\mathrm{S},1180}$ (10 %) indicates an uncertainty range of retrieved τ of ± 0.2 which is well within the uncertainty range of WALES. The mean τ inferred from the mini-DOAS off-nadir observations is significantly lower than measured by SMART and mini-DOAS nadir measurements. This may result from different field of view of the off-nadir geometry that does not observe the same clouds as SMART and nadir channels did. With the scanning sensors orientated to starboard the off-nadir retrieval corresponds to cirrus 8 km east of the flight track. As the MODIS satellite image in Fig. 12 indicates, the cirrus becomes thinner towards east, which agrees with the lower values of τ provided by the mini-DOAS off-nadir retrieval.

Figure 14 (b) displays a zoom of the time series between 08:20 UTC to 08:24 UTC. During this flight segment, τ inferred by WALES is characterized by systematic oscillations varying between 0.2 and 1.1 also visible in the backscatter profile of WALES in Fig. 13. The lag time between two maxima is approximately between 20 s and 25 s flight time, which corresponds to a horizontal distance between 4.4 km and 5.5 km. This pattern is present in the measurements of SMART, WALES and the mini-DOAS nadir channels even though a little bit obscured in the latter measurements due to its reduced time resolution. Overall the comparison provides evidence that the inferred τ agrees between the sensors.

Figure 15 (a) and Fig. 15 (b) show scatter plots of retrieved τ for the different instruments. A linear regression through the origin is performed. Data where a second cloud layer was present below the cirrus (gray points) are excluded. The comparison between SMART and WALES in Fig. 15 (a) shows that the majority of the data is below the 1:1 line (gray). The linear regression results in $f(x) = 0.6621 \cdot x$. The regression confirms that SMART systematically retrieves higher values of τ compared to WALES. The scattered data points lie below the regression and the majority of data are likely still contaminated by a second cloud layer (gray points) that effects the SMART retrieval but are not include in the WALES retrieval.

Compared to SMART, mini-DOAS nadir spectrometers observations of τ depart less from WALES (Fig. 15 (b)). Similar to SMART, the slope of the linear fit $f(x) = 0.6943 \cdot x$ indicates that mini-DOAS systematically overestimates τ compared to WALES. This similarity between SMART and mini-DOAS is obvious as SMART and mini-DOAS rely on the same radiometric calibration.

5.3 Probability distribution of cirrus optical thickness

For further comparison the frequency of occurrence (PDF) of τ retrieved by SMART, mini-DOAS nadir spectrometers and WALES is investigated. The PDFs are shown in Fig. 16. Corresponding mean and median values of the distributions are given in Tab. 4. SMART (black solid line) and mini-DOAS (gray solid line) almost show the same PDF indicating that both instruments measured the same cloud area. In both cases observed τ range from 0.15 to 1.25 for SMART and mini-DOAS and from 0.15 to 0.7 for WALES. The PDF maxima for SMART and mini-DOAS is around $\tau = 0.4$, slightly more pronounced for the mini-DOAS. For both instruments, the PDFs are squeed to small τ with a median of 0.47 for SMART and 0.48 for mini-DOAS. It is slightly smaller than the mean value of 0.5 for SMART and 0.51 for mini-DOAS. Both PDFs are long-tailed towards large τ, slowly decreasing to higher values of τ. In contrast, τ measured by WALES (black dashed line) shows a

Atmos. Chem. Phys. Discuss., doi:10.5194/acp-2016-970, 2016
Manuscript under review for journal Atmos. Chem. Phys.
Published: 4 November 2016

Atmospheric Chemistry and Physics Discussions

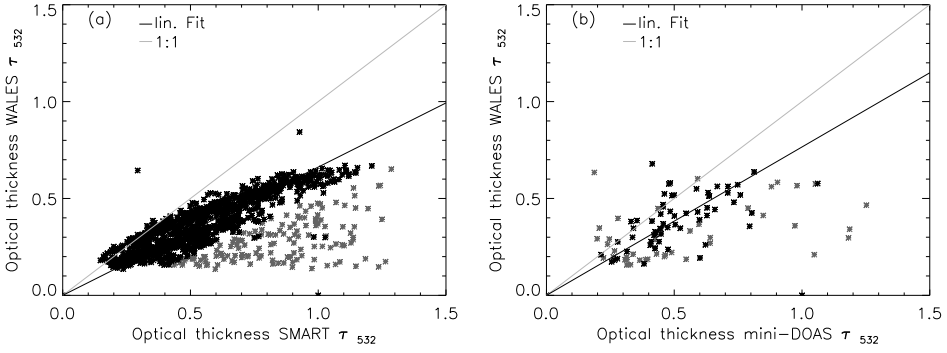

Figure 15. (a) Comparison of the retrieved cirrus optical thickness τ by WALES and SMART at λ = 532 nm wavelength. (b) Comparison of the retrieved cirrus optical thickness τ by WALES and mini-DOAS at λ = 532 nm wavelength. Measurements when a second cirrus layer was present are displayed in grey and are discarded in the regression.

Table 4. Mean and median of the PDFs of cirrus optical thickness τ derived from WALES, SMART and mini-DOAS.

	mean	median
WALES	0.35	0.33
SMART	0.56	0.52
mini-DOAS	0.52	0.47

stronger shift to low τ as the mean value of τ is significantly lower. The most frequent τ was around $\tau = 0.2$. The WALES measurement do not show τ larger than 0.7 what results in a stronger decrease of of the WALES PDF to higher τ compared to SMART and mini-DOAS. The difference may be explained by different field of view and therefore measuring different horizontal parts of the clouds. It is assumed, that SMART and mini-DOAS, e.g. due to similar large FOV, measure additional scattered radiation and are influenced by three dimensional radiative effects caused by clouds, atmosphere and surface, which are not considered in the presented 1-dimensional RTS and the iterative retrieval. Differences in τ may also result from the measurement methodologies. While WALES uses active remote sensing with a laser, SMART and mini-DOAS are passive remote instruments relaying on scattered sunlight. Therefore, SMART and mini-DOAS are influenced by the RT of the whole atmosphere, while WALES is only sensitive to scattering within its narrow LOS. Additionally, the vertical probing of the cloud also depends on the used wavelength. While WALES uses backscatter measurements at λ = 532 nm and λ = 1064 nm the retrieval by SMART and mini-DOAS is performed at λ = 1180 nm.

Atmos. Chem. Phys. Discuss., doi:10.5194/acp-2016-970, 2016
Manuscript under review for journal Atmos. Chem. Phys.
Published: 4 November 2016

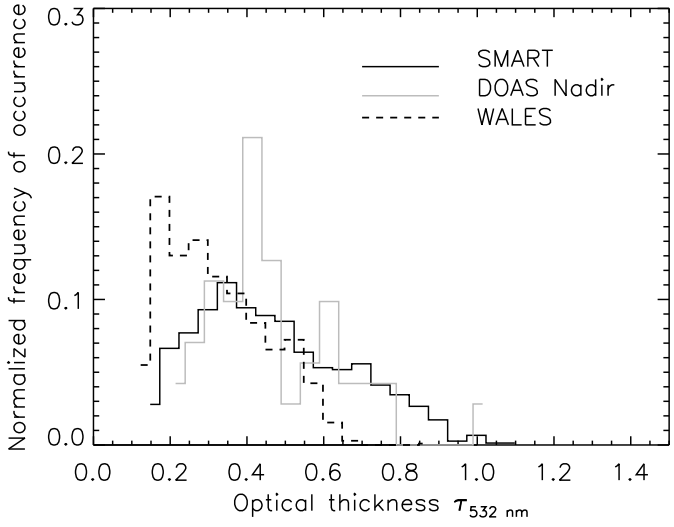

Figure 16. PDFs of cirrus optical thickness τ at $\lambda = 532$ nm retrieved from SMART, mini-DOAS and WALES measurement. The bin size is 0.05 units of τ.

6 Conclusions

The potential of airborne radiance measurements in off-nadir direction for cirrus remote sensing is investigated. For this purpose RTS are performed and airborne measurements of the Spectral Modular Airborne Radiation measurement sysTem (SMART) and the Differential Optical Absorption Spectrometer (mini-DOAS) are compared. A sensitivity study based on RTS showed that off-nadir measurements are generally more suited for detecting and investigating optically thin cirrus and SVC than observations in nadir orientation. Using off-nadir observations the sensitivity of measured upward radiance I^{L} is larger than for nadir measurements up to a factor of 10 depending on the details of the observation geometry and cloud properties. The RTS indicate that large observation angles θ_{L} (close to the horizon) and small relative solar azimuth angle ϕ (observations in direction of the Sun) result in the highest sensitivity. Additionally, the smoothing of horizontal variability of optical thickness-fields by off-nadir observations has also been shown.

For retrievals of cirrus optical thickness τ using off-nadir measurements, the wavelength selection is crucial. Simulations indicate that wavelength larger than $\lambda = 900$ nm are best suited. While reflected I^{L} of smaller wavelength is significantly contaminated by scattering and absorption due to atmospheric molecules. Furthermore, the off-nadir orientation reduces the influence of the surface albedo α on reflected I^{L}.

Similarly, a reasonable good assumption of the ice crystal shape used in the RTS is important. In off-nadir geometry the shape effects on reflected I^{L} are more pronounced than for nadir measurements. An incorrect assumption will bias the retrieval of

Atmos. Chem. Phys. Discuss., doi:10.5194/acp-2016-970, 2016
Manuscript under review for journal Atmos. Chem. Phys.
Published: 4 November 2016

Atmospheric Chemistry and Physics Discussions

τ significantly. On the other hand, the sensitivity for different ice crystal shapes may offer the possibility to retrieve shape information when measuring at different viewing angles.

In order to apply a radiance based cloud retrieval to off-nadir measurements of mini-DOAS during ML-CIRRUS, the raw measurements are radiometrically calibrated. For this purpose a cross-calibration between SMART and mini-DOAS nadir and off-nadir channels is performed to calculate calibrated I_{mD} from mini-DOAS raw counts. A comparison of ML-CIRRUS measurements shows that calibrated upward I_{mD} of mini-DOAS is within the uncertainty range of SMART. Individual cross-calibrations from different campaigns and flights revealed, that the calibrations can be transferred to different flights within one campaign providing that no technical adjustments are performed. However, considering the uncertainty and limitations of such cross-calibrations, a laboratory radiometric calibration of the mini-DOAS is recommended to improve the uncertainties of the cloud retrieval and to allow measurements independent to SMART.

Using the SMART, mini-DOAS nadir and scanning sensor measurements in conjunction with an iterative retrieval τ is derived for a case study of ML-CIRRUS. For individual retrieval, the inferred τ from SMART, mini-DOAS and the additional lidar measurement by the Water Vapour Lidar Experiment in Space (WALES) show a reasonable good agreement in τ for the nadir channels with absolute differences of ± 0.22 ($66.6\,\%$) between SMART and WALES and ± 0.17 ($52.3\,\%$) between mini-DOAS and WALES observations respectively. The retrieval using mini-DOAS scanning channels is also successful demonstrated for a reduced set of observations limited to θ_{L} between $85°$ and $90°$. Differences in τ range up to ± 0.73 between SMART and mini-DOAS off-nadir observations are caused by the different viewing geometries. While the scanning telescopes view into starboard direction thus probing the cirrus cloud top at approximately 8000 m aside the flight track. However, the case study shows that cirrus retrieval using airborne off-nadir observations with mini-DOAS are possible and can increase the potential of remote sensing on HALO. For future dedicated cloud observations it is recommended to adjust θ_{L} to the most sensitive direction between $60°$ and $90°$ to reduce the uncertainty in the off-nadir retrieval. Additional off-nadir scans in homogeneous cloud conditions might be used to estimate the cirrus ice crystal shape and minimize the retrieval uncertainties.

Acknowledgements. This research was funded by the German Research Foundation (DFG, HALO-SPP 1294). The authors acknowledge the support by the Deutsche Forschungsgemeinschaft (DFG) through grants PF 384/7-1/2, PF 384/16-1 and WE 1900/35-1. The authors thank the pilots and appreciate the support by the Flugbereitschaft of the German Aerospace Center (DLR). Additionally the authors thank enviscope GmbH for preparation and testing of SMART.

Atmos. Chem. Phys. Discuss., doi:10.5194/acp-2016-970, 2016
Manuscript under review for journal Atmos. Chem. Phys.
Published: 4 November 2016

Atmospheric Chemistry and Physics Discussions

References

Baum, B. A., Heymsfield, A. J., Yang, P., and Bedka, S. T.: Bulk scattering properties for the remote sensing of ice clouds. Part I: Microphysical data and models, J. Appl. Meteor., 44, 1885–1895, 2005.

Bierwirth, E., Wendisch, M., Ehrlich, A., Heese, B., Tesche, M., Althausen, D., Schladitz, A., Müller, D., Otto, S., Trautmann, T., Dinter, T., von Hoyningen-Huene, W., and Kahn, R.: Spectral surface albedo over Morocco and its impact on the radiative forcing of Saharan dust, Tellus, 61B, 252–269, 2009.

Bourassa, A. E., Degenstein, D. A., and Llewellyn, E. J.: Climatology of the subvisual cirrus clouds as seen by OSIRIS on Odin, Adv. Space Res., 36, 807–812, doi:http://dx.doi.org/10.1016/j.asr.2005.05.045, 2005.

Bozzo, A., Maestri, T., Rizzi, R., and Tosi, E.: Parameterization of single scattering properties of mid-latitude cirrus clouds for fast radiative transfer models using particle mixtures, Geophys. Res. Lett., 35, L16 809, 2008.

Brückner, M., Pospichal, B., Macke, A., and Wendisch, M.: A new multispectral cloud retrieval method for ship-based solar transmissivity measurements, J. Geophys. Res. Atmos., 119, 11.338–11.354, doi:10.1002/2014JD021775, 2014.

Chen, T., Rossow, W., and Zhang, Y.: Radiative effects of cloud-type variations, J. Climate, 13, 264–286, 2000.

Clark, R. N., Swayze, G. A., Wise, R., Livo, E., Hoefen, T., Kokaly, R., and Sutley, S. J.: USGS digital spectral library splib06a, Tech. rep., U.S. Geological Survey, http://speclab.cr.usgs.gov/spectral-lib.html, 2007.

Comstock, J. M., Ackerman, T. P., and Mace, G. G.: Ground-based lidar and radar remote sensing of tropical cirrus clouds at Nauru Island: Cloud statistics and radiative impacts, J. Geophys. Res., 107, 4714, doi:10.1029/2002JD002203, 2002.

Cziczo, D. J., Froyd, K. D., Hoose, C., Jensen, E. J., Diao, M., Zondlo, M. A., Smith, J. B., Twohy, C. H., and Murphy, D. M.: Clarifying the Dominant Sources and Mechanisms of Cirrus Cloud Formation, Science, doi:10.1126/science.1234145, 2013.

Davis, S., Hlavka, D., Jensen, E., Rosenlof, K., Yang, Q. O., Schmidt, S., Borrmann, S., Frey, W., Lawson, P., Voemel, H., and Bui, T. P.: In situ and lidar observations of tropopause subvisible cirrus clouds during TC4, J. Geophys. Res., 115, D00J17, doi:10.1029/2009JD013093, 2010.

Delanoe, J., Protat, A., Jourdan, O., Pelon, J., Papazzoni, M., Dupuy, R., Gayet, J.-F., and Jouan, C.: Comparison of Airborne In Situ, Airborne Radar-Lidar, and Spaceborne Radar-Lidar Retrievals of Polar Ice Cloud Properties Sampled during the POLARCAT Campaign, J. Atmos. Oceanic Technol., 30, 57–73, doi:10.1175/JTECH-D-11-00200.1, 2013.

Ehret, G., Gross, S., Schäfler, A., Wirth, M., Fix, A., and Kiemle, C.: Characterization of Cirrus Cloud Properties by Airborne Differential Absorption and High Spectral Resolution Lidar Measurements, AGU Fall Meeting Abstracts, 2014.

Eichler, H., Ehrlich, A., Wendisch, M., Mioche, G., Gayet, J.-F., Wirth, M., Emde, C., and Minikin, A.: Influence of ice crystal shape on retrieval of cirrus optical thickness and effective radius: A case study, J. Geophys. Res., 114, D19203, doi:doi:10.1029/2009JD012215, 2009.

Eloranta, E. W.: Practical model for the calculation of multiply scattered lidar returns, Appl. Opt., 37, 2464–2472, doi:10.1364/AO.37.002464, 1998.

Esselborn, M., Wirth, M., Fix, A., Tesche, M., and Ehret, G.: Airborne high spectral resolution lidar for measuring aerosol extinction and backscatter coefficients, Appl. Opt., 47, 346–358, doi:10.1364/AO.47.000346, 2008.

Frey, W., Borrmann, S., Kunkel, D., Weigel, R., de Reus, M., Schlager, H., Roiger, A., Voigt, C., Hoor, P., Curtius, J., Krämer, M., Schiller, C., Volk, C. M., Homan, C. D., Fierli, F., Di Donfrancesco, G., Ulanovsky, A., Ravegnani, F., Sitnikov, N. M., Viciani, S., D'Amato, F., Shur, G. N., Belyaev, G. V., Law, K. S., and Cairo, F.: In situ measurements of tropical cloud properties in the West African Mon-

soon: upper tropospheric ice clouds, Mesoscale Convective System outflow, and subvisual cirrus, Atmos. Chem. Phys., 11, 5569–5590, doi:10.5194/acp-11-5569-2011, http://www.atmos-chem-phys.net/11/5569/2011/, 2011.

Fricke, C., Ehrlich, A., Jäkel, E., Bohn, B., Wirth, M., and Wendisch, M.: Influence of local surface albedo variability and ice crystal shape on passive remote sensing of thin cirrus, Atmos. Chem. Phys., 14, 1943–1958, doi:10.5194/acp-14-1943-2014, 2014.

Froyd, K. D., Murphy, D. M., Lawson, P., Baumgardner, D., and Herman, R. L.: Aerosols that form subvisible cirrus at the tropical tropopause, Atmos. Chem. Phys., 10, 209–218, doi:10.5194/acp-10-209-2010, 2010.

Fu, Q. and Liou, K.: Parameterization of the radiative properties of cirrus clouds, J. Atmos. Sci., 50, 2008–2025, 1993.

Fu, Q., Hu, Y., and Yang, Q.: Identifying the top of the tropical tropopause layer from vertical mass flux analysis and CALIPSO lidar cloud observations, Geophys. Res. Lett., 34, doi:10.1029/2007GL030099, l14813, 2007.

Gross, S., Forster, L., Wirth, M., Schäfler, A., Freudenthaler, V., Fix, A., and Mayer, B.: Characterization of mid-latitude cirrus cloud with airborne and ground-based lidar measurements during ML-CIRRUS, in: EGU General Assembly Conference Abstracts, vol. 17 of *EGU General Assembly Conference Abstracts*, p. 10283, 2015.

Gueymard, C. A.: The sun's total and spectral irradiance for solar energy applications and solar radiation models, Solar Energy, 76, 423–453, 2004.

Hüneke, T.: Aufbau und Charakterisierung eines sechsfach–miniDOAS–Spektrographen für das Forschungsflugzeug DLR-HALO, Master's thesis, Ruprecht-Karls-University Heidelberg, 2011.

IPCC: Climate Change 2013: The Physical Science Basis, Cambridge University Press, 2013.

Jensen, E. J., Pfister, L., Jordan, D. E., Bui, T. V., Ueyama, R., Singh, H. B., Thornberry, T., Rollins, A. W., Gao, R.-S., Fahey, D. W., Rosenlof, K. H., Elkins, J. W., Diskin, G. S., DiGangi, J. P., Lawson, R. P., Woods, S., Atlas, E. L., Rodriguez, M. A. N., Wofsy, S. C., Pittman, J., Bardeen, C. G., Toon, O. B., Kindel, B. C., Newman, P. A., McGill, M. J., Hlavka, D. L., Lait, L. R., Schoeberl, M. R., Bergman, J. W., Selkirk, H. B., Alexander, M. J., Kim, J.-E., Lim, B. H., Stutz, J., and Pfeilsticker, K.: The NASA Airborne Tropical TRopopause EXperiment (ATTREX): High-Altitude Aircraft Measurements in the Tropical Western Pacific, BAMS, doi:10.1175/BAMS-D-14-00263.1, http://dx.doi.org/10.1175/BAMS-D-14-00263.1, 2015.

Kärcher, B.: Properties of subvisible cirrus clouds formed by homogeneous freezing, Atmos. Chem. Phys., 2, 161–170, doi:10.5194/acp-2-161-2002, 2002.

King, M. D., Platnick, S., Yang, P., Arnold, G. T., Gray, M. A., Riedi, J. C., Ackerman, S. A., and Liou, K. N.: Remote sensing of liquid water and ice cloud optical thickness and effective radius in the Arctic: Application of airborne multispectral MAS data, J. Atmos. Oceanic Technol., 21, 857–875, 2004.

Klepp, C., Ament, S., Bakan, S., Hirsch, L., and Stevens, B.: NARVAL Campaign Report, vol. 164, Reports on Earth System Science, Max Planck Institute for Meteorology Hamburg, Germany, 2014.

Lampert, A., Ehrlich, A., Dörnbrack, A., Jourdan, O., Gayet, J.-F., Mioche, G., Shcherbakov, V., Ritter, C., and Wendisch, M.: Microphysical and radiative characterization of a subvisible midlevel Arctic ice cloud by airborne observations - a case study, Atmos. Chem. Phys., 9, 2647–2661, 2009.

Lee, J., Yang, P., Dessler, A. E., Gao, B.-C., and Platnick, S.: Distribution and radiative forcing of tropical thin cirrus clouds, J. Atmos. Sci., 66, 3721–3731, doi:10.1175/2009JAS3183.1, 2009.

Mayer, B. and Kylling, A.: Technical note: The *libRadtran* software package for radiative transfer calculations - description and examples of use, Atmos. Chem. Phys., 5, 1855–1877, 2005.

McFarquhar, G. M., Heymsfield, A. J., Spinhirne, J., and Hart, B.: Thin and subvisual tropopause tropical cirrus: Observations and radiative impacts, J. Atmos. Sci., 57, 1841–1853, doi:10.1175/1520-0469(2000)057, 2000.

Nakajima, T. and King, M.: Determination of the optical thickness and effective particle radius of clouds from reflected solar radiation measurements. Part I: Theory, J. Atmos. Sci., 47, 1878–1893, 1990.

Oikarinen, L.: Effect of surface albedo variations on UV-visible limb-scattering measurements of the atmosphere, J. Geophys. Res., doi:10.1029/2001JD001492, 2002.

Ou, S., Liou, K., Gooch, W., and Takano, Y.: Remote sensing of cirrus cloud parameters using advanced very-high-resolution radiometer 3.7- and 10.9-μm channels, Appl. Opt., 32, 2171–2180, 1993.

Ou, S., Liou, K.-N., Takano, Y., Rao, X., Fu, Q., Heymsfield, A., Miloshevich, L., Baum, B., and Kinne, S.: Remote sounding of cirrus cloud optical depths and ice crystal structures from AVHRR data: Verification using FIRE II IFO measurements, J. Atmos. Sci., 52, 4143–4158, 1995.

Pierluissi, J. and Peng, G.-S.: New molecular transmission band models for LOWTRAN, Opt. Eng., 24, 541–547, 1985.

Platt, C.: Remote sounding of high clouds. III: Monte Carlo calculations of multiple-scattered lidar returns, J. Atmos. Sci., 38, 156–167, 1981.

Platt, U. and Stutz, J.: Differential Optical Absorption Spectroscopy: Principles and Applications, Series: Physics of Earth and Space Environments, Springer Verlag, ISBN: 3540211934, 2008.

Pruppacher, H. and Klett, J.: Microphysics of Clouds and Precipitation, Kluwer Academic, 1997.

Rolland, P. and Liou, K.: Surface variability effects on the remote sensing of thin cirrus optical and microphysical properties, J. Geophys. Res., 106, 22 965–22 977, 2001.

Rolland, P., Liou, K., King, M., Tsay, S., and McFarquhar, G.: Remote sensing of optical and microphysical properties of cirrus clouds using Moderate-Resolution Imaging Spectroradiometer channels: Methodology and sensitivity to physical assumptions, J. Geophys. Res., 105, 11 721–11 738, 2000.

Sassen, K., Wang, Z., and Liu, D.: Cirrus clouds and deep convection in the tropics: Insights from CALIPSO and CloudSat, J. Geophys. Res. Atmos., 114, doi:10.1029/2009JD011916, 2009.

Sausen, R., Isaksen, I., Grewe, V., Hauglustaine, D., Lee, D., Myhre, G., Köhler, M., Pitari, G., Schumann, U., Stordal, F., and Zerefos, C.: Aviation radiative forcing in 2000: An update on IPCC (1999), Meteor. Z., 14, 555–561, 2005.

Schäfer, M., Bierwirth, E., Ehrlich, A., Heyner, F., and Wendisch, M.: Retrieval of cirrus optical thickness and assessment of ice crystal shape from ground-based imaging spectrometry, Atmos. Meas. Tech., 6, 1855–1868, doi:10.5194/amt-6-1855-2013, 2013.

Sen, P. K.: Estimates of the Regression Coefficient Based on Kendall's Tau, J. Am. Stat. Assoc., 63, 1379–1389, doi:10.1080/01621459.1968.10480934, 1968.

Shettle, E.: Models of aerosols, clouds and precipitation for atmospheric propagation studies, in: Atmospheric propagation in the uv, visible, ir and mm-region and related system aspects, no. 454 in AGARD Conference Proceedings, 1989.

Stamnes, K., Tsay, S.-C., Wiscombe, W., and Laszlo, I.: DISORT, a General-Purpose Fortran Program for Discrete-Ordinate-Method Radiative Transfer in Scattering and Emitting Layered Media: Documentation of Methodology, Tech. rep., Dept. of Physics and Engineering Physics, Stevens Institute of Technology, Hoboken, NJ 07030, 2000.

Theil, H.: A Rank–Invariant Method of Linear and Polynomial Regression Analysis, in: Henri Theils Contributions to Economics and Econometrics, edited by Raj, B. and Koerts, J., vol. 23 of *Adv. S. Theo. App. Eco.*, pp. 345–381, Springer Netherlands, doi:10.1007/978-94-011-2546-8_20, 1992.

Toon, O. B., Starr, D. O., Jensen, E. J., Newman, P. A., Platnick, S., Schoeberl, M. R., Wennberg, P. O., Wofsy, S. C., Kurylo, M. J., Maring, H., Jucks, K. W., Craig, M. S., Vasques, M. F., Pfister, L., Rosenlof, K. H., Selkirk, H. B., Colarco, P. R., Kawa, S. R., Mace, G. G., Minnis, P., and Pickering, K. E.: Planning, implementation, and first results of the Tropical Composition, Cloud and Climate Coupling Experiment (TC4), J. Geophys. Res. Atmos., 115, doi:10.1029/2009JD013073, 2010.

Twomey, S. and Seton, K. J.: Inferences of gross microphysical properties of clouds from spectral reflectance measurements, J. Atmos. Sci., 37, 1065–1069, 1980.

Voigt, C., Schumann, U., Minikin, A., Abdelmonem, A., Afchine, A., Borrmann, S., Boettcher, M., Buchholz, B., Bugliaro, L., Costa, A., Curtius, J., Dollner, M., Dörnbrack, A., Dreiling, V., Ebert, V., Ehrlich, A., Fix, A., Forster, L., Frank, F., Fütterer, D., Giez, A., Graf, K., Grooß, J.-U., Groß, S., Heimerl, K., Heinold, B., Hüneke, T., Järvinen, E., Jurkat, T., Kaufmann, S., Kenntner, M., Klingebiel, M., Klimach, T., Kohl, R., Krämer, M., Krisna, T. C., Luebke, A., Mayer, M., Mertes, S., Molleker, S., Petzold, A., Pfeilsticker, K., Port, M., Rapp, M., Reutter, P., Rolf, C., Rose, D., Sauer, D., Schäfler, A., Schlage, R., Schnaiter, M., Schneider, J., Spelten, N., Spichtinger, P., Stock, P., Walser, A., Weigel, R., Weinzierl, B., Wendisch, M., Werner, F., Wernli, H., Wirth, M., Zahn, A., Ziereis, H., and Zöger, M.: ML-CIRRUS – The airborne experiment on natural cirrus and contrail cirrus with the high-altitude long-range research aircraft HALO, Bulletin of the American Meteorological Society, doi:10.1175/BAMS-D-15-00213.1, 2016.

Wang, P.-H., Minnis, P., McCormick, M. P., Kent, G. S., and Skeens, K. M.: A 6–year climatology of cloud occurrence frequency from Stratospheric Aerosol and Gas Experiment II observations (1985–1990), J. Geophys. Res. Atmos., 101, 29 407–29 429, doi:10.1029/96JD01780, http://dx.doi.org/10.1029/96JD01780, 1996.

Wendisch, M., Müller, D., Schell, D., and Heintzenberg, J.: An airborne spectral albedometer with active horizontal stabilization, J. Atmos. Oceanic Technol., 18, 1856–1866, 2001.

Wendisch, M., Pilewskie, P., Pommier, J., Howard, S., Yang, P., Heymsfield, A. J., Schmitt, C. G., Baumgardner, D., and Mayer, B.: Impact of cirrus crystal shape on solar spectral irradiance: A case study for subtropical cirrus, J. Geophys. Res., 110, Art. No. D03 202, 2005.

Wendisch, M., Yang, P., and Pilewskie, P.: Effects of ice crystal habit on thermal infrared radiative properties and forcing of cirrus, J. Geophys. Res., 112, D03 202, doi:10.1029/2006JD007899, 2007.

Wendisch, M., Pöschl, U., Andreae, M. O., Machado, L. A. T., Albrecht, R., Schlager, H., Rosenfeld, D., Martin, S. T., Abdelmonem, A., Afchine, A., Araujo, A., Artaxo, R., Aufmhoff, H., Barbosa, H. M. J., Borrmann, S., Braga, R., Buchholz, B., Cecchini, M. A., Costa, A., Curtius, J., Dollner, M., Dorf, M., Dreiling, V., Ebert, V., Ehrlich, A., Ewald, F., Fisch, G., Fix, A., Frank, F., Fütterer, D., Heckl, C., Heidelberg, F., Hüneke, T., Jäkel, E., Järvinen, E., Jurkat, T., Kanter, S., Kästner, U., Kenntner, M., Kesselmeier, J., Klimach, T., Knecht, M., Kohl, R., Kölling, T., Krämer, M., Krüger, M., Krisna, T. C., Lavric, J. V., Longo, K., Mahnke, C., Manzi, A. O., Mayer, B., Mertes, S., Minikin, A., Molleker, S., Münch, S., Nillius, B., Pfeilsticker, K., Pöhlker, C., Roiger, A. E., Rose, D., Rosenow, D., Sauer, D., Schnaiter, M., Schneider, J., Schulz, C., de Souza, R. A. F., Spanu, A., Stock, P., Vila, D., Voigt, C., Walser, A., Walter, D., Weigel, R., Weinzierl, B., Werner, R., Yamasoe, M. A., Ziereis, H., Zinner, T., and Zöger, M.: The ACRIDICON-CHUVA campaign: Studying tropical deep convective clouds and precipitation over Amazonia using the new German research aircraft HALO, Bull. Am. Meteorol. Soc., doi:10.1175/BAMS-D-14-00255.1, 2016.

Wiensz, J. T., Degenstein, D. A., Lloyd, N. D., and Bourassa, A. E.: Retrieval of subvisual cirrus cloud optical thickness from limb-scatter measurements, Atmos. Meas. Tech., 6, 105–119, doi:10.5194/amt-6-105-2013, 2013.

Winker, D. M. and Trepte, C. R.: Laminar cirrus observed near the tropical tropopause by LITE, Geophys. Res. Lett., 25, 3351–3354, 1998.

Wirth, M., Fix, A., Mahnke, P., Schwarzer, H., Schrandt, F., and Ehret, G.: The airborne multi-wavelength water vapor differential absorption lidar WALES: System design and performance, Applied Physics B-Lasers And Optics, 96, 201–213, 2009.

Atmos. Chem. Phys. Discuss., doi:10.5194/acp-2016-970, 2016
Manuscript under review for journal Atmos. Chem. Phys.
Published: 4 November 2016

Atmospheric Chemistry and Physics Discussions

Woodbury, G. E. and McCormick, M. P.: Zonal and geographical distributions of cirrus clouds determined from SAGE data, J. Geophys. Res. Atmos., 91, 2775–2785, doi:10.1029/JD091iD02p02775, 1986.

Yang, H. Y., Dobbie, S., Herbert, R., Connolly, P., Gallagher, M., Ghosh, S., Al-Jumur, S. M. R. K., and Clayton, J.: The effect of oberserved vertical structure, habits, and size distribution on the solar radiative properties and cloud evolution of cirrus clouds, Quart. J. R. Met. Soc., 138, 1221–1232, 2012.

Yang, P., Bi, L., Baum, B. A., Liou, K. N., Kattawar, G. W., Mishchenko, M. I., and Cole, B.: Spectrall consistent scatterin, absorption, and polarization properties of atmospheric ice crystals at wavelengths from 0.2 to 100 μm, J. Atmos. Sci., 70, 330–347, 2013.

Zhang, Y., Macke, A., and Albers, F.: Effect of crystal size spectrum and crystal shape on stratiform cirrus radiative forcing, Atmos. Res., 52, 59–75, 1999.